Measurement 224 (2024) 113853

Contents lists available at ScienceDirect

Measurement

journal homepage: www.elsevier.com/locate/measurement

Topography measurement methods evaluation for entire bending-fatigued fracture surfaces of specimens obtained by explosive welding

Przemysław Podulka [a], Wojciech Macek [b,*], Dariusz Rozumek [c], Krzysztof Żak [d], Ricardo Branco [e]

[a] Faculty of Mechanical Engineering and Aeronautics, Rzeszow University of Technology, Powstancow Warszawy 12, 35-959 Rzeszów, Poland
[b] Faculty of Mechanical Engineering and Ship Technology, Gdańsk University of Technology, Narutowicza 11/12, 80-233 Gdańsk, Poland
[c] Department of Mechanics and Machine Design, Opole University of Technology, Mikołajczyka 5, 45-271 Opole, Poland
[d] Faculty of Mechanical Engineering, Opole University of Technology, Mikołajczyka 5, 45-271 Opole, Poland
[e] Department of Mechanical Engineering, University of Coimbra, CEMMPRE, ARISE, 3030-788 Coimbra, Portugal

ARTICLE INFO

Keywords:
Explosive welding
Cyclic bending
Surface topography
Entire fracture surface
High-frequency noise
Data thresholding

ABSTRACT

In this paper, the methods of compensation of differences in the results of entire bending-fatigued fracture surface topographies were presented. The roughness evaluation was performed with a focus variation microscope and confocal surface topography measurement techniques. The differences in the ISO 25178 roughness parameters were investigated and procedures for their compensation were studied. It was found that various types of optical measurements can cause differences in the errors occurring in the measurement process, such as outliers, and noise. The reduction of differences in the various optical roughness measurements can be attained when measurement errors are compensated. For this study, the applications of general procedures available in commercial software can be suitable for improvements of the roughness measurement results, such as raw data thresholding technique, digital filtering (S-filter), power spectral density, and autocorrelation function analyses. The validation of measurement techniques was proposed for areal and profile studies, including analysis of differences in the calculation areal ISO 25178 roughness parameters.

1. Introduction

Analysis of topography, including the calculation of roughness parameters, is crucial in many surface characterisations. An accurate description of surface performance can be essential in the analysis of many properties. A very popular area of research is tribological performance, where wear resistance in coatings is influenced by the accuracy of surface roughness assessments, as introduced by Rosenkranz et al. [1]. Padha et al. [2], in their studies on adhesive and abrasive wear, reported that when a softer surface slides against a smoothed and rough surface, respectively, it is reflected in the analysis of the surface topography. Magri et al. [3] established a correlation between the surface topography of milled materials and their wear during hot forging. Vázquez et al. [4] showed that the geometry of the microgrooves, which is strongly related to the surface topography analysis, improved lubricant retention by increasing the liquid expansion. Maruda et al. [5] used the roughness in sliding applications and concluded that the maximum valley depths (parameter *Sv* of ISO 25178 standard) were related to the oil retention in the recesses of the machined surfaces. Yao et al. [6] found the control of surface roughness especially crucial when machining high-strength alloy materials. Zakharov et al. [7] also found the control of surface roughness as a pivotal variable in the characterisation of the roundness errors. Le et al. [8] noted that nearly 1,500 papers have been published on the topic of surface texturing and its impact on tribological performance over the last two decades. Abdel-Aal [9] highlighted a promising synergy between tribology and biology. The field of orthopaedic surgery in the bioimplant industry has also been comprehensively reviewed by Shen et al. [10]. Vishnoi et al. [11] connected surface texturing with improved tribological performance, emphasizing factors such as anti-biofouling hydrophobicity and load-carrying capacity. Mao et al. [12] conducted an extensive review of recent advancements in laser surface texturing (LST) to enhance the tribological properties of engineering materials, discussing both current challenges and future directions. Historically, the tribological performance of the surface roughness measurement was improved in contact mechanics, especially in applications related to the wear of materials [13].

* Corresponding author.
E-mail addresses: p.podulka@prz.edu.pl (P. Podulka), wojciech.macek@pg.edu.pl (W. Macek), d.rozumek@po.edu.pl (D. Rozumek), k.zak@po.edu.pl (K. Żak), ricardo.branco@dem.uc.pt (R. Branco).

https://doi.org/10.1016/j.measurement.2023.113853
Received 14 October 2023; Received in revised form 1 November 2023; Accepted 11 November 2023
Available online 13 November 2023

Nomenclature

A_5	Elongation, %
ACF	autocorrelation function
AM	additive manufacturing
Diff_1	variation in parameters received by the two measurement methods
Diff_2	deviation obtained before and after thresholding for the FVM technique
Diff_3	deviation obtained before and after thresholding for the confocal method
Diff_4	deviation for data after thresholding calculated between FVM and confocal measurements
Diff_5	deviation calculated for FVM and confocal measurements after data pre-processing
Diff_6	deviation obtained for FVM measurement before and after 15 μm S-filtering
Diff_7	deviation obtained for confocal measurement before and after 15 μm S-filtering
Diff_8	deviation calculated for FVM and confocal measurements after 15 μm S-filtering
D_f	fractal dimension
E	elastic modulus, GPa
FVM	focus variation microscopy
h	wave height
HSI	hyperspectral imaging
L	interface line length
LST	laser surface texturing
N_f	fatigue life
NMPs	non-measured points
PSD	power spectral density
PSI	phase shifting interferometric microscopy
S-filter	filter removing small-scale components
XCT	X-ray computed tomography
σ_y	yield stress, MPa
σ_{us}	ultimate tensile stress, MPa
Sa	arithmetic mean height, μm
Sal	auto-correlation length, mm
Sdq	root mean square gradient
Sdr	developed interfacial areal ratio, %
Sk	core roughness depth, μm
Sku	kurtosis
Smc	inverse areal material ratio, μm
Smr	areal material ratio, %
Sp	maximum peak height, μm
Spk	reduced summit height, μm
Sq	root mean square height, μm
Smrk1	upper bearing area, %
Smrk2	lower bearing area, %
Ssk	skewness
Std	texture direction, °
Str	texture parameter
Sxp	extreme peak height, μm
Sv	maximum valley depth, μm
Svk	reduced valley depth, μm
Sz	the maximum height of the surface, μm
Vm	material volume, $\mu m^3/\mu m^2$
Vmc	core material volume, $\mu m^3/\mu m^2$
Vmp	peak material volume, $\mu m^3/\mu m^2$
Vv	void volume, $\mu m^3/\mu m^2$
Vvc	core void volume, $\mu m^3/\mu m^2$
Vvv	pit void volume, $\mu m^3/\mu m^2$

Table 1
Chemical composition of the tested materials (wt.%) [52].

Mat.	C	Si	Mn	P	S	N	Al	Cu	Cr	Ni	Mo	V	Ti	Nb
P355NH	0.18	0.33	1.23	0.012	0.001	0.003	0.038	0.19	0.03	0.21	0.003	0.003	0.003	0.02
	C	S	Cr	Ni	Mn	Si	Mo	Nb	Cu	Fe	P	V	W	Co
C-276	0.004	0.002	16.00	57.96	0.47	0.04	15.71	0.01	0.01	5.78	0.004	0.13	3.39	0.26
	C	Si	Mn	P	S	Cr	Ni	Mo	Cu	N				
SAF2507	0.015	0.37	0.83	0.026	0.01	24.90	6.86	3.79	0.33	0.250				

Table 2
Static properties of the tested materials [52].

Materials	σ_y, MPa	σ_{us}, MPa	E, GPa	A_5, %
P355NH	415	555	212	30
C-276	481	762	205	62
SAF2507	806	914	199	31

Table 3
Characteristics of joint parameters [52].

Materials	λ, μm	h, μm	L, μm
P355NH + C-276	583.93	137.90	8581.47
P355NH + SAF2507	518.14	130.49	7905.49

Topography and roughness are not only used to study the mechanical properties of a surface, but also in many other analyses, including the strength of materials. Jacobs et al. [14] considered vacancies, interstitials, and substitutional defects and found that they were closely related to the microstructure of the surface and had a critical impact on the material strength. The full understanding of these relationships is currently a great challenge in the field of materials science. The contact strength of bearings, investigated by Zhou [15] using a micro–macro contact model, was characterised considering roughness, waviness and profile analyses. Macek et al. [16] examined the fracture surface topographies to account for the effect of asynchronous axial–torsional strain-controlled loading. Garcias et al. [17] used surface topography analysis to compare the mechanical behaviour of tool steels produced via selective laser melting and conventional manufacturing processes. More recently, Żak et al. [18] connected surface topography features with surface functionality.

Topography analysis of fracture surfaces caused by fatigue loading is very common in literature because it can provide important clues on the failure mechanisms. Kobayashi and Shockey [19] correlated fatigue behaviour under multiaxial loading with the topography characteristics of fracture surfaces. Molent et al. [20] effectively connected the fractal geometry with crack growth. Dependences of surface topography parameters and multiaxial fatigue damage were reported by Macek et al. [21]. Sampath et al. [22] evaluated the fracture events from crack initiation to final fracture under slow strain rates based on fracture

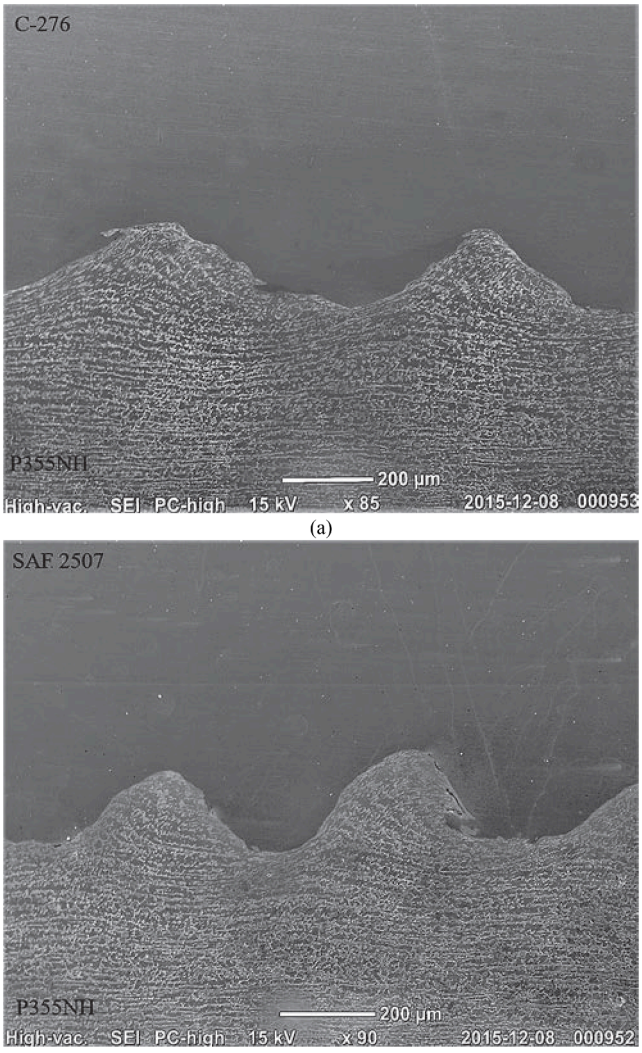

Fig. 1. Example specimen joints: a) P355NH + C-276, b) P355NH + SAF2507 [40].

surface topography data. The concept of fractal dimension, as discussed by Carpinteri et al. [23] in their work, serves as a pivotal approach for connecting normalized fatigue strength with force amplitude, and it remains a very popular research line in this field. Ţălu et al. [24] evaluated the fractal behaviour at both micro or nanoscales using fractal succolarity, fractal lacunarity, and surface entropy.

A variety of fatigue fracture surface studies have been conducted based on surface topography characterisation. Beyene et al. [25] investigated the bending fatigue failure mechanisms considering fracture surface analyses. Zhang et al. [26] proposed surface geometrical examination for bending fatigue failure analysis in a micro straight bevel gear. Macek [27] advocated that fracture surface topography parameters are influenced by the type of loading in aluminium alloys subjected to combined bending-torsion. The fatigue behaviour of Ti6Al4V titanium alloys produced by laser-beam powder bed fusion also exhibited considerable influence on surface topography [28]. Fracture surface topography in austenitic steel plates subjected to repeated bending was studied by Tanaka et al. [29] using fracture mechanics concepts.

An accurate surface topography assessment relies on several factors. Historically, the measurement of surface roughness was first conducted by tactile methods which are able to detect the depth information of surfaces, as discussed by Shin et al. [30]. Later, considerable advances in measuring techniques took place with the introduction of optical methods. This approach, as stated by Whitehouse [31], is 'probably the most useful optical instrument' for measuring surfaces, films, and coatings. The clear dominance of the optical methods is the time of measuring which is much faster than a stylus. Kaplonek et al. [32] indicated it as essential in production systems when time is shortened. Due to the reduction in production costs, industries worldwide are increasingly exploring innovative solutions involving clad materials. These solutions typically involve a cost-effective base material with a more expensive overlay material [53]. Clad materials prove to be well-suited to meet these requirements, especially when addressing corrosive or chemical environments, or aiming to reduce weight [54]. This approach involves the utilization of a cheaper material as the base, which is then overlaid with a protective layer resistant to aggressive environments and various types of radiation, among others. In such materials, a thin layer of the applied material effectively protects the base material, which is often carbon or low-alloy steel. These materials find extensive application in the chemical, energy, and shipbuilding industries.

Despite many definite advantages, the accuracy of the optical methods depends on a number of factors. One important type of error is related to the non-measured points (NMPs). Increasing the intensity of the light may not be a suitable solution. It can cause an increase in the values of height, hybrid and functional ISO 25178 parameters, as studied by Pawlus et al. in [33]. Liu et al. [34] analysed the origin of the NMPs by comparing both focus variation microscopy (FVM) and X-ray computed tomography (XCT) when inspecting the surface texture of additively manufactured (AM) products. It was reported that NMPs were found around some deep features, like grooves and particles, starting by filling in NMPs by neighbour interpolation.

Individual peaks, also known as outliers or spikes, are the errors in the optical measurements that most influence the ISO 25178 height parameters. Ismail et al. [35] proposed an outlier correction based on the median relative height of the surrounding data points. Podulka et al. [36] used methods based on standard deviation and root mean square slope and compared them to the morphological closing filter considering a structuring element of horizontal plane shape and a thresholding method. Huang et al. [37] implemented a fast and robust algorithm to process surface data with outliers and defects. In all of the above studies, the main challenge in the outlier suppression was the classification of the point data as an unwanted element. False estimation of bandwidth for spike reduction can remove important surface features.

The measurement noise, therefore, is a further type of error included in the raw measured surface topography data. From the ISO standards [38], measurement noise can be defined as the noise added to the output signal when the normal use of a measuring instrument occurs. According to Maculotti et al. [39], noise has different sources, it can be internally generated, but it also has many external sources associated with the environment. Generally, the measurement noise can be analysed by selecting an adequate bandwidth, as suggested by De Groot in [40]. High-frequency measurement errors are one of the most important noise problems, which are, in many cases, caused by vibrations [41]. Commonly used surface metrology filtration techniques based on the Gaussian function did not always provide reasonable results, as demonstrated by Sun et al. [42] or Zakharchenko [43]. In a different study, Podulka [44] compared the regular method for noise suppression taking into account the size, density and distribution features. However, excluding statistical and averaging methods, the analysis of measurement noise is still a challenging task.

To measure surface roughness, two methods were employed and compared. The FVM technique is characterised by very high vertical resolution, easy specimen preparation, and the ability to provide quantified surface topography and roughness evaluation with true-color images [45]. It excels in measurement efficiency, repeatability, traceability, and speed. In addition, it does have limitations in the measurement of surfaces with steep angles [46]. On the contrary, confocal methods have limitations related to pixel resolution and the size of the

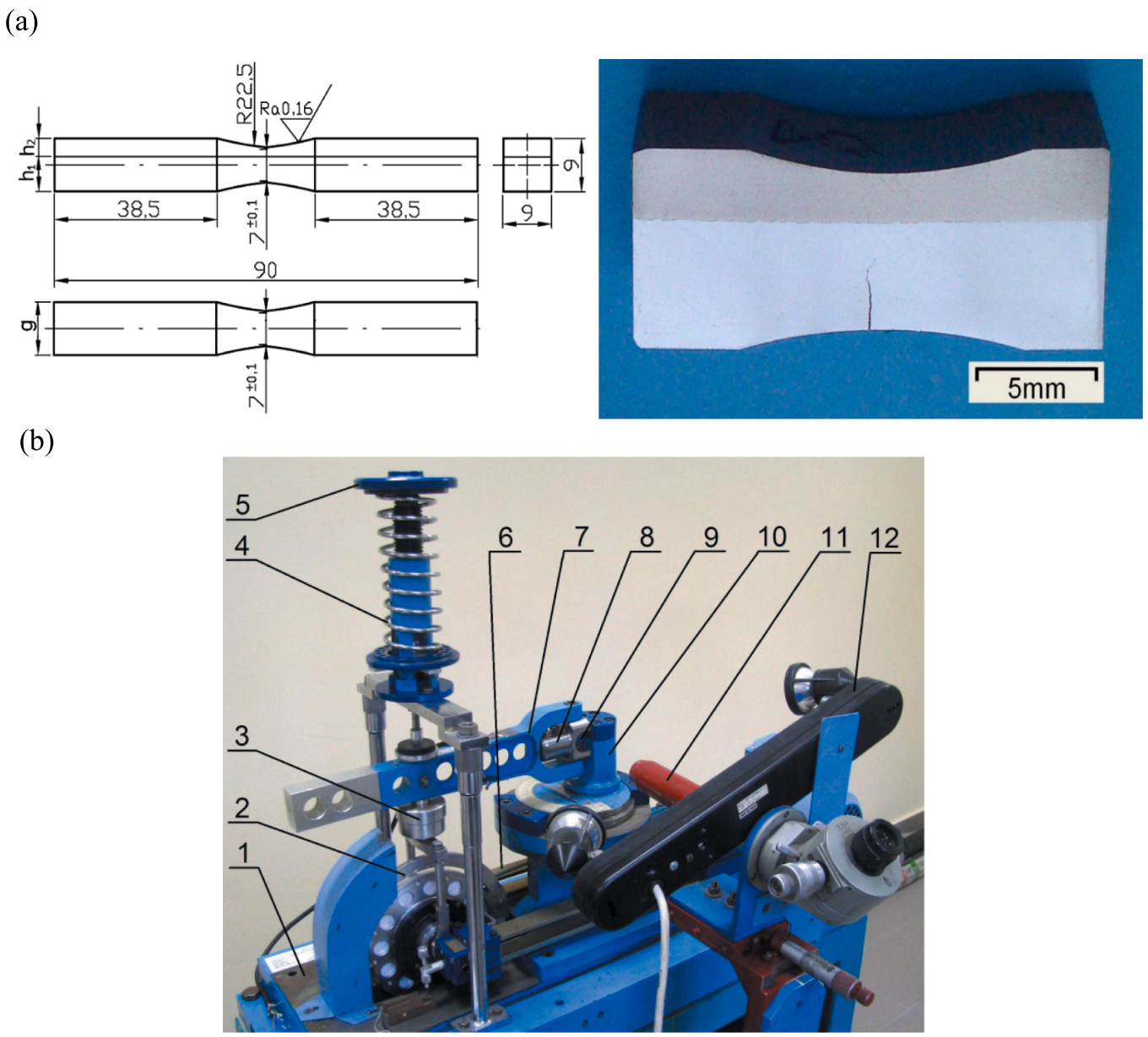

Fig. 2. (a) Specimens used in fatigue tests (units: mm); (b) fatigue test stand MZGS-100; where: 1 – machine base, 2 – disks for load application, 3 – vibration damper, 4 – spring, 5 – actuator (static load), 6 – flat springs, 7 – lever (effective length = 200 mm), 8 – holder, 9 – specimen, 10 – rotational head with a clamp, 11 – telescope, 12 – lighting.

scanned area [47]. However, unlike phase-shifting interferometric (PSI) microscopy, confocal methods are not restricted to smoother surfaces and can capture detailed information on rougher ones [48]. Nevertheless, confocal measurements are susceptible to scattering noise at steep angles and background noise from specular reflection on optical elements [49]. Concerning the analysis of the morphology of surface details, hyperspectral technology has proven to be highly beneficial [50]. Hyperspectral imaging (HSI), which combines spectroscopy and 2D imaging [51], can provide in-depth insight into sample composition and properties, making it invaluable for characterizing fracture surfaces resulting from bending-fatigue loading.

In this paper, the accuracy of the outlier and noise reduction is studied. Then, the results obtained with both, FVM and confocal measurement methods are detailed compared. The entire bending-fatigued fracture surface topographies were considered with an application of various methods for the data processing, such as digital filters, functions and analyses of isometric views of measured details.

With regard to the paper's structure, Section 2, which is divided into three subsections, describes the organization of the materials and methods. Subsection 2.1 addresses the experiments, encompassing details such as material composition, testing equipment, and specimen geometry. Subsection 2.2 presents the parameters for surface topography measurement used for each technique. Subsection 2.3 focuses on explaining the applied methods and functions used in the description of surface roughness. The comprehensive step-by-step procedure is outlined in Subsection 2.4, accompanied by a flow chart depicting the proposed experiment. In relation to Section 3 devoted to the presentation and discussion of results, the first subsection addresses the proposed procedure and the outliers, while the second subsection tackles the mitigation of high-frequency measurement noise. Finally, the main findings are summarized in the last section.

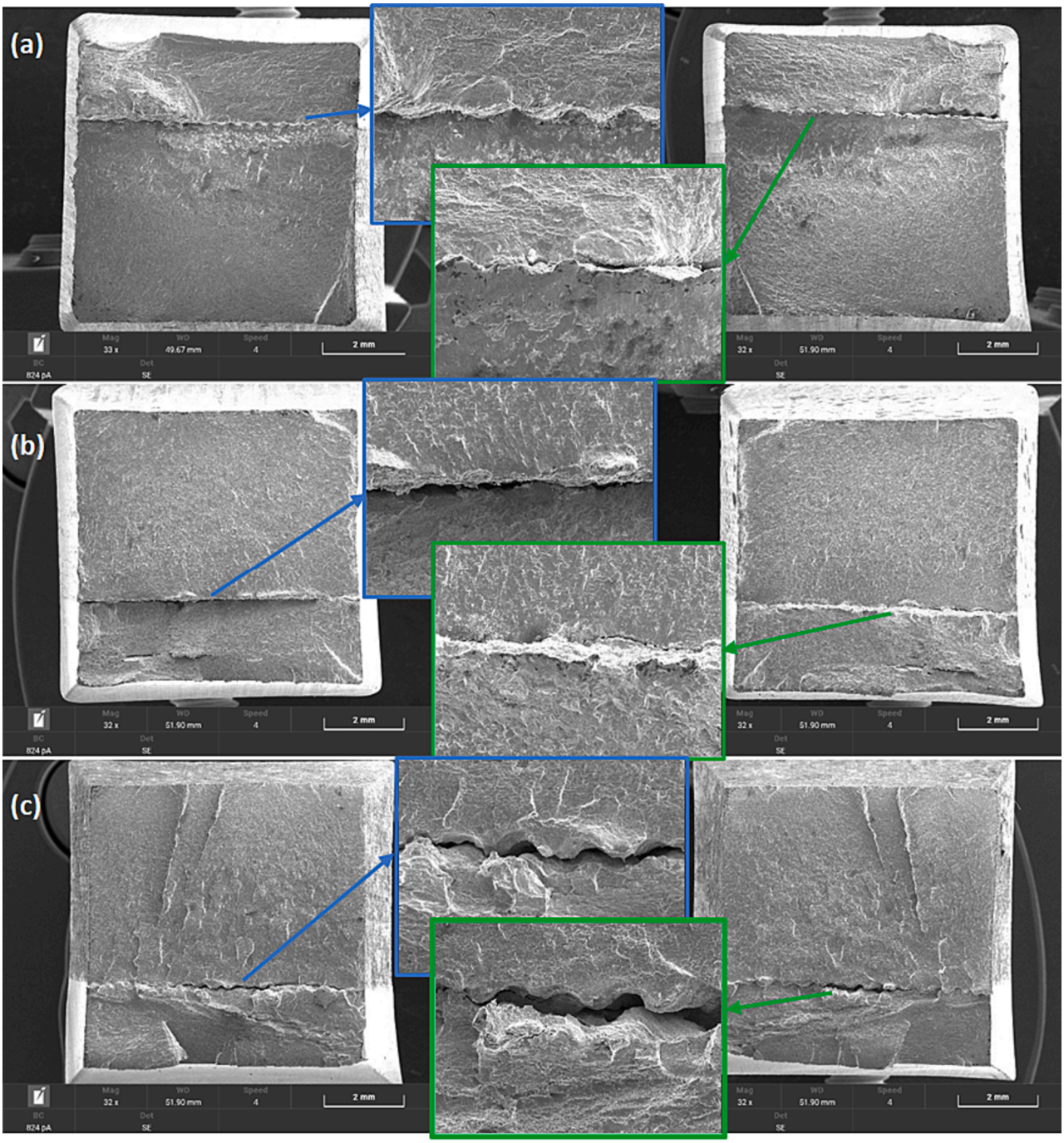

Fig. 3. SEM fractography for the entire fracture surface (for both sides of the broken specimens): (a) specimen no. 1, (b) specimen no. 2 and (c), specimen no. 3.

2. Materials and methods

2.1. Analysed surfaces and parameters calculated

Specimens cut from plates used in explosion welding by EXPLOMET High-Energy Techniques Works Company were tested. The base material was a 10 mm thick P355NH carbon steel plate, and the clad materials were nickel alloy C-276 and super duplex SAF 2507, with a thickness of 3 mm, deposited on the steel. The chemical composition of the materials before cladding, obtained from the certificate attached to the material, is presented in Table 1 while the main static properties are described in Table 2 [52].

After the cladding process was done, ultrasonic testing was conducted to check whether a given element was fully connected without defects. Then, the joint of each specimen was observed and the joint parameters (wavelength λ, wave height h, interface line length L [53]) were determined. The measured average values of the parameters for the tested joints clad materials are given in Table 3.

Each joint was characterized by a different wave structure, as shown in Fig. 1. In the case of the P355NH + C-276 specimen, the joint was characterized by a low wave with sharp joint outlines (Fig. 1a), while the P355NH + SAF 2507 steel (Fig. 1b) was characterized by a higher wave with a gentler vertex than one of the previously described specimens.

The specimens were subjected to metallographic examination using a light microscope, OLYMPUS IX40 model, and a scanning electron microscope, Jeol Neoscope II JCM-6000 model. A computer image analysis system, LECO IA 32 model, was used to determine the parameters of joint waves generated in explosion welding [54].

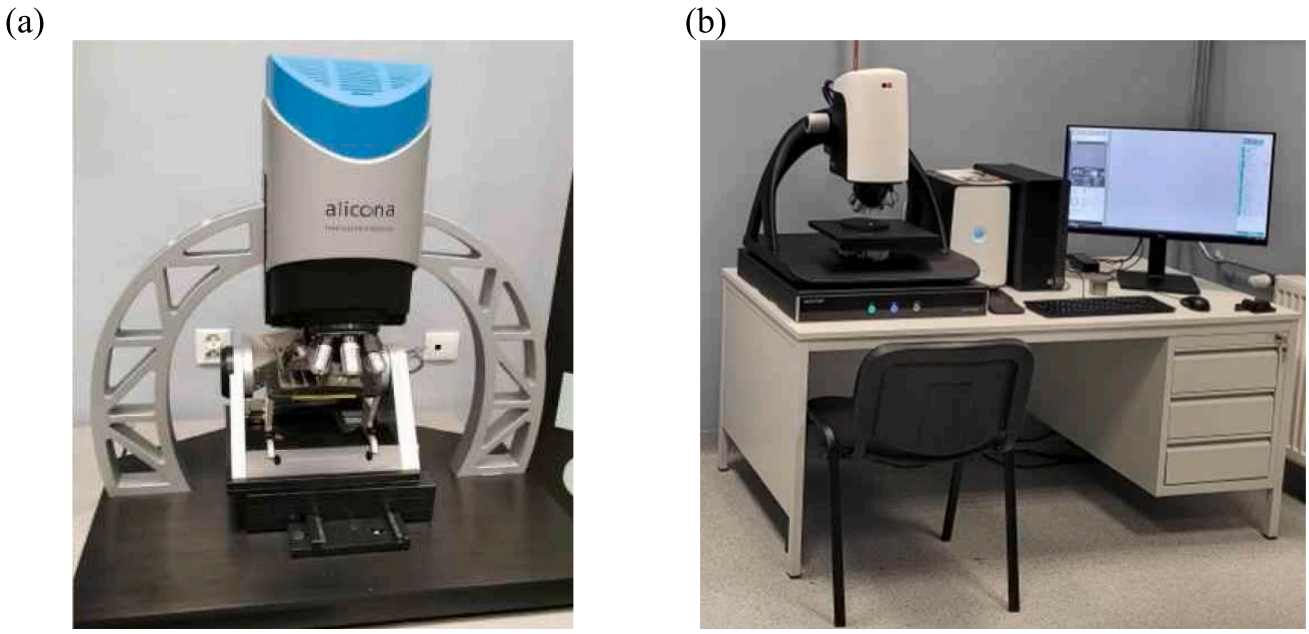

Fig. 4. Surface measurement devices: (a) Alicona IF G5 model and (b) Sensofar 3D optical profilometer (S-Neox).

Tensile tests showed that the strength of the base material, in all cases, after cladding increased from 555 MPa to 590 MPa. However, the strength of the applied materials C-276 and SAF2507, after cladding, decreased from 762 and 866 MPa to 584 and 590 MPa, respectively. The tensile strength of bimetals should be from a minimum of 490 MPa to a maximum of 630 MPa, in accordance with EN-PN ISO6892-1. In the remaining tests, such as the shear test (DIN50162) and the bend test (EN13445-2), the requirements were met. The results of all tests met the recommendations outlined in the standards, which means that the connection between the two materials was correct.

The base material used is P355NH steel, known for its weldability and suitability for high-temperature operations. Regarding the cladding materials, the selected ones were C-276 (a nickel alloy) and SAF2507 (a super-duplex stainless steel). These materials have a high content of chromium (16 % and 24.9 %, respectively) and nickel (57.96 % and 6.86 %, respectively) which make them hard and brittle. The base material has a strength of 555 MPa, while the applied materials have strengths of 762 MPa (C-276) and 914 MPa (SAF2507). The observed variations can be explained by the fact that the strength of the base material increases when combined with overlaid materials due to the higher tensile strengths of the overlaid materials. Conversely, the reduction in strength of the overlaid materials results from the lower strength of the base material.

Fatigue bending tests were performed in the high-cycle and low-cycle fatigue range with a load ratio R = -1 and a load frequency of 28.4 Hz. For each specimen, the tests were performed for three bending moments (M_a): 17.18, 19.41, and 24.5 N·m. Specimens 1 and 3 were made of P355NH + SAF2507 and were tested at a bending moment of 17.18 N·m (no. 1) and 24.5 N·m (no. 3). Specimen 2 (P355NH + C-276) was tested at 19.41 N·m (no. 2). The tests were carried out on the MGZS-100 fatigue machine (see Fig. 2b) [55] at the Opole University of Technology. The machine enables the execution of cyclic bending, torsion, and bending-torsion scenarios. The cracks were measured with a micrometre using an optical microscope with a magnification of 25 ×. The shape and dimensions of the specimen are shown in Fig. 2 [54]. In the fatigue-tested specimens, the ratio of the net height of the base material to the height of the applied material was h_1: h_2 = 2.5: 1.

The entire bending-fatigued fracture surfaces were analysed considering isometric views of the surface and the calculation of ISO 25178 roughness parameters. Over 20 probes were measured and examined. To minimize uncertainties, the measurements were not repeated. However, the proposed procedure was based on the analysis of variations in roughness parameters obtained from measurements conducted using two different instruments. The post-failure analyses of topographies, namely those based on the entire fracture surface, can contribute to the comprehensive knowledge of the failure mechanisms, as described in detail by Macek [27,56]. The fracture surfaces of the specimens were measured using focus variation microscopy (FVM), from which the data sets with a large depth of field observation can be obtained. A study based on the entire fracture surface carried out using ISO 25178 height and functional (volume) parameters, connected with the fractal dimension, can be potentially decisive in the accuracy of the analysis.

Thus, the use of the optical surface roughness measurement method of the entire fracture, e.g. using FVM, in connection with relevant areal ISO25178 parameters, can be encouraging in the estimation of the causes of damage. However, even if the precise surface roughness measurement technique is applied, the data processing methods can be selected erroneously. In this way, the accuracy of the whole study can be lost, as investigated by Podulka et al. [57].

The examination of fracture surfaces by scanning electron microscopy (SEM) can provide interesting clues on the failure mechanisms. Fig. 3 displays the micrographs taken with a Tescan Vega 4 microscope for both sides of the broken specimens.

The ISO 25178 surface roughness parameters considered in this study were divided into the following groups: height (amplitude), functional, spatial, hybrid, functional (volume) and material ratio curves. The eight differences (from *Diff_1* to *Diff_8*) in the values were obtained by comparing both techniques applying digital processing methods, like outlier removal and high-frequency noise reduction.

For a more sophisticated characterisation of the bending-fatigued fracture surfaces, the analysis of the profiles (2D) was put on an equal plane with the areal (3D) analysis. It was demonstrated that the assessment of profiles over the entire fracture surface is crucial in the analysis of fatigue life (N_f) [16].

2.2. Measurement process

All analysed surfaces were measured with focus variation microscopy and confocal techniques. The Focus Variation Method (FVM) was

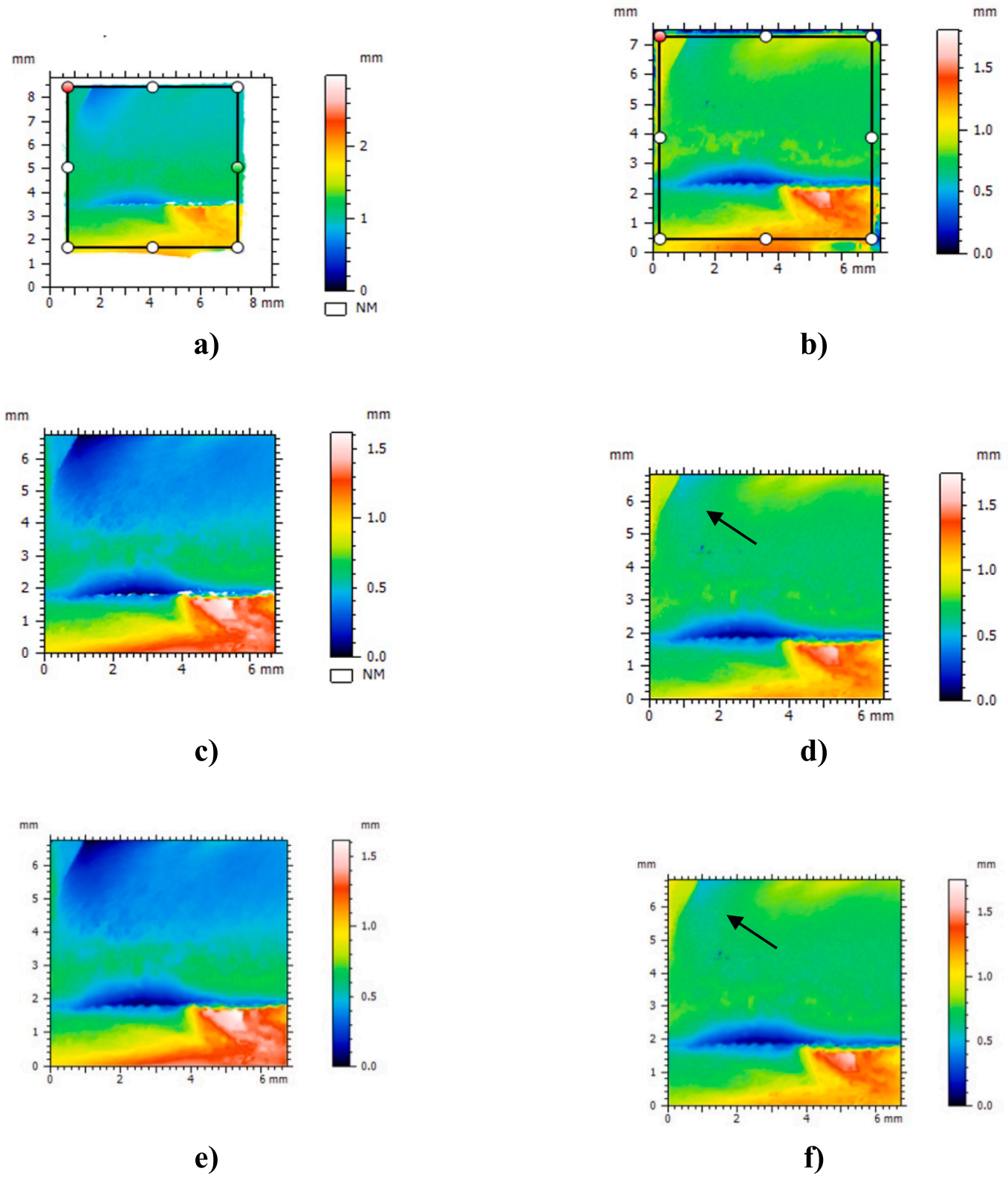

Fig. 5. Contour maps: raw measured data (a,b), extracted analysed area (c,d) and extracted area with fulfilled NMPs (e,f) of the entire bending-fatigued fracture surface (specimen no. 1) measured with focus variation microscopy (left column) and confocal (right column) methods.

applied, using an Alicona IF G5 model (see Fig. 4a), to determine the surface geometry of fractures. The area was 8.852 mm × 8.857 mm with 5021 × 5024 measured points, and spacing of 1.763 μm, respectively. The measuring instrument was equipped with a Nikon EPI lens with 10 × magnification.

The entire fracture area measurement method was applied using a Sensofar 3D optical profilometer (S-Neox) with 10 × magnification (see Fig. 4b). The measurement length was 7.431 mm × 7.162 mm with 5386 × 5191 measured points and spacing equal to 1.380 μm. The ISO 25178 surface topography parameters were calculated and analysed

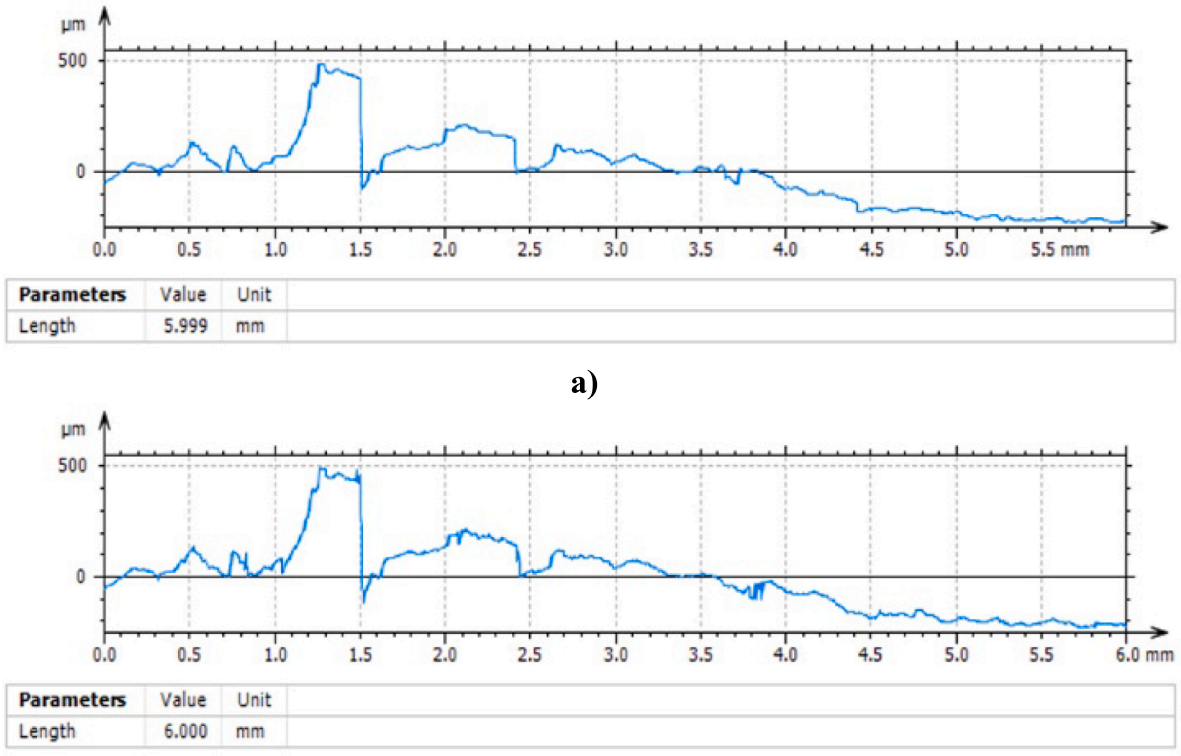

Fig. 6. Surface topography profiles extracted from the entire bending-fatigued fracture surface (specimen no. 3) with focus variation microscopy (a) and confocal (b) methods.

using Digital Surf MountainsMap software.

The most noticeable differences regarding an analysis based on the isometric view of the surface, see Fig. 5, were related to: the maximum height of the data (by comparing the left and right columns); the presence of the NMPs (Fig. 5a and Fig. 5c); and the outliers, indicated by arrows in Fig. 5d and Fig. 5f. The presence of spikes and measurement noise were also marked for profiles in Fig. 6.

The proposed methodology is based on the differences in the two contactless surface roughness measurement techniques. The repetition of the measurement process was not approved, as the main purpose was to identify the high-frequency noise within the variations in the collected data. The main methodology highlights the variations as the primary factor affecting the accuracy of the results obtained. One measuring method cannot enhance the accuracy of the other; however, mitigating these differences would broaden the occurrence of the specific type of measurement errors selected. Thus, this proposal led to the adoption of a procedure for reducing high-frequency noise by minimising variations in those measurement aspects influenced by the presence of the identified errors.

2.3. Applied methods for the compensation of the differences in the measurement results

Most of the differences in the results of surface roughness measurements by focus variation microscopy and confocal methods were observed in terms of the number (and density) of the NMPs gathered usually in different areas of the surface. Further, the individual peaks tend to increase the amplitude parameters, usually in the *Sz* and *Sk* curves. The third type of error is the noise located in the high-frequency domain. Surface data received after the focus variation microscopy measurement included some NMPs. Those data were fulfilled by a method based on the mean value of the neighbour points. Removing this type of optical measurement error is crucial because it can cause a false estimation of skewness (*Ssk*) [33].

Surface data obtained by confocal measurement have some individual peaks, as previously presented in Fig. 5. This type of optical error significantly affects the height (amplitude) parameters. It was found that individual peaks were also introduced as outliers [35] or spikes [36]. One of the methods for their suppression is the robust filter [37]. However, extraction of the spike data with robust methods was burdened with errors related to the removal of various features. In general, inappropriate application of digital filters can affect the removal of unwanted elements with those relevant to surface roughness characterisation. Contrary to surface data filtering techniques, algorithms based on the deviation or slope can be successfully used [36]. Many encouraging results for data suppression were presented by Jiang et al. [58] based on the thresholding technique which refers to a family of segmentation methods. This approach was found especially suitable when the reduction in time of the data processing is important.

Fig. 7 displays the entire bending-fatigued fracture surface for both topography measurement methods. Some differences can be found by direct isometric view analysis, like those indicated by the arrows (Fig. 7a and Fig. 7b). However, considering the properties of the surface, the ISO 25178 roughness parameters were also determined. All of the differences in ISO 25178 surface topography parameters were smaller than 5 %, except for the hybrid parameters *Sdq* and *Sdr*, around 80 % and 170 %, respectively, and for the functional parameter *Smr,* about 100 %.

The reduced core roughness *Sk* also increased usually between 5 % and 10 %. Increasing values of the root mean square gradient *Sdq*, developed interfacial areal ratio *Sdr*, areal material ratio *Smr* and, as mentioned, *Sk* parameters can indicate an enlargement in the selected type of measurement errors.

The hybrid parameters were classified as those vulnerable to the occurrence of high-frequency measurement errors, studied

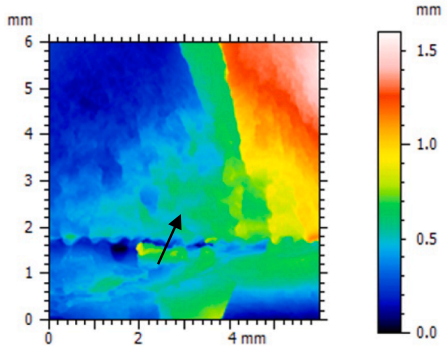

a)

Height parameters		
Sq	0.3376	mm
Ssk	0.9432	
Sku	3.116	
Sp	1.045	mm
Sv	0.5574	mm
Sz	1.602	mm
Sa	0.2637	mm
Functional parameters		
Smr	0.00009493	%
Smc	0.5713	mm
Sxp	0.3456	mm
Spatial parameters		
Sal	1.077	mm
Std	177.0	°
Hybrid parameters		
Sdq	3.145	
Sdr	39.29	%
Functional parameters (Volume)		
Vm	0.01607	mm³/mm²
Vv	0.5874	mm³/mm²
Vmp	0.01607	mm³/mm²
Vmc	0.3032	mm³/mm²
Vvc	0.5731	mm³/mm²
Vvv	0.01429	mm³/mm²
Functional parameters (Stratified surfaces)		
Sk	0.7045	mm
Spk	0.6018	mm
Svk	0.05285	mm
Smr1	19.22	%
Smr2	98.29	%

c)

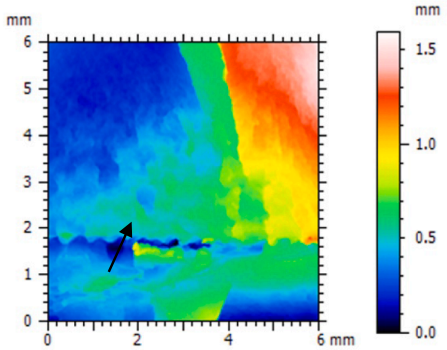

b)

Height parameters		
Sq	0.3260	mm
Ssk	0.9533	
Sku	3.158	
Sp	1.018	mm
Sv	0.5757	mm
Sz	1.593	mm
Sa	0.2530	mm
Functional parameters		
Smr	0.00019030	%
Smc	0.5532	mm
Sxp	0.3367	mm
Spatial parameters		
Sal	1.077	mm
Std	176.7	°
Hybrid parameters		
Sdq	5.671	
Sdr	105.6	%
Functional parameters (Volume)		
Vm	0.01573	mm³/mm²
Vv	0.5689	mm³/mm²
Vmp	0.01573	mm³/mm²
Vmc	0.2913	mm³/mm²
Vvc	0.5546	mm³/mm²
Vvv	0.01427	mm³/mm²
Functional parameters (Stratified surfaces)		
Sk	0.6462	mm
Spk	0.6060	mm
Svk	0.05543	mm
Smr1	19.58	%
Smr2	94.71	%

d)

Fig. 7. Isometric views (a,b) and ISO 25178 parameters (c,d), respectively, received from the entire bending-fatigued fracture surface (specimen no. 3) measured with focus variation microscopy (a,c) and confocal (b,d) methods.

comprehensively by Pawlus et al. in [59]. It was found that the presence of the measurement noise can cause errors greater than 100 % in the *Sdq* and *Sdr* parameter values.

In most cases, depending on the type of analysed surface, the *Smr* and *Sk* parameters were also influenced by the measurement noise [60]. From that issue, the differences in focus variation microscopy and confocal measurement results can indicate that the second method can contain a high-frequency measurement noise.

For confocal measurements, the high-frequency components were received in some areas, like 2.6—2.9 mm area in the profile length, indicated by arrows in Fig. 8. It was also found that the edge areas of analysed details often contained high-frequency data, like presented enlargement in profiles from Fig. 9.

An example of the high-frequency data introduced for profiles and their extracted areas is exhibited in Fig. 10. It was found that the high-frequency components were gathered in some profile length, except at the end of the studied data. The frequency distribution of the data for the enlarged profile areas was investigated by the power spectral density (PSD) graphs. For the confocal measurement (Fig. 10e and Fig. 10f), the dominant frequency (59 μm) was located in the high-frequency domain but for the focus variation microscopy measurement (Fig. 10c and Fig. 10d) the value of the dominant wavelength (299 μm) did not indicate the presence of the high-frequency errors or those errors were negligible.

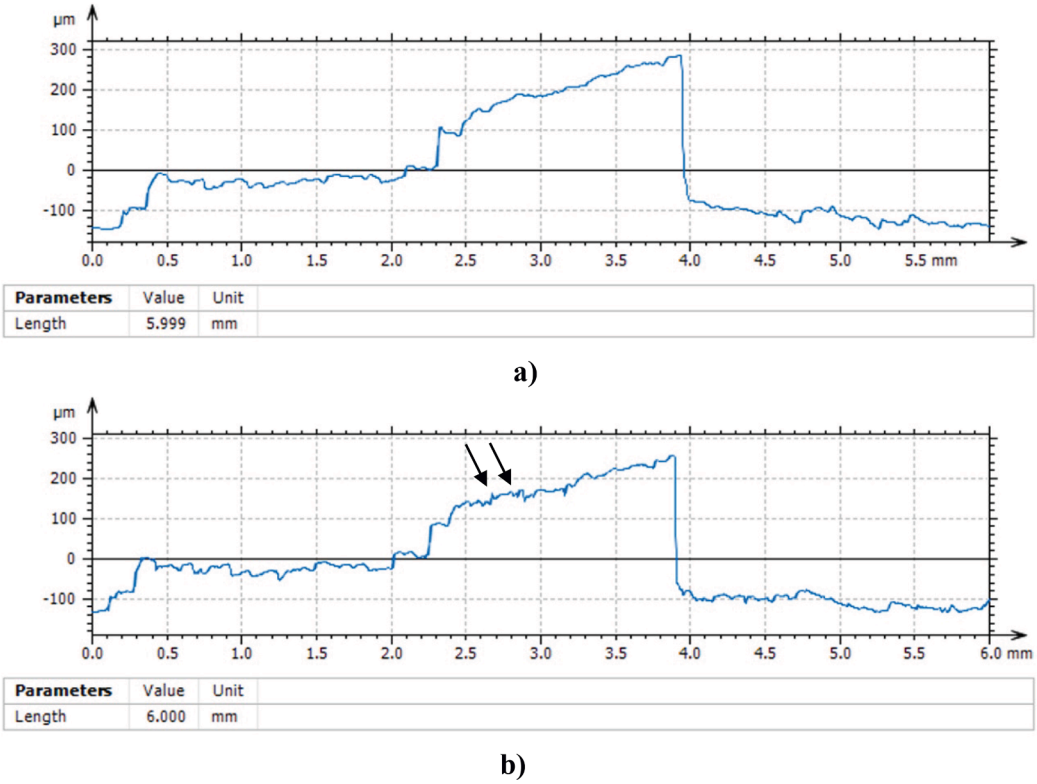

Fig. 8. Profiles extracted from entire bending-fatigued fracture surface topography (specimen no. 3) received after measurement by focus variation microscopy (a) and confocal (b) types of equipment.

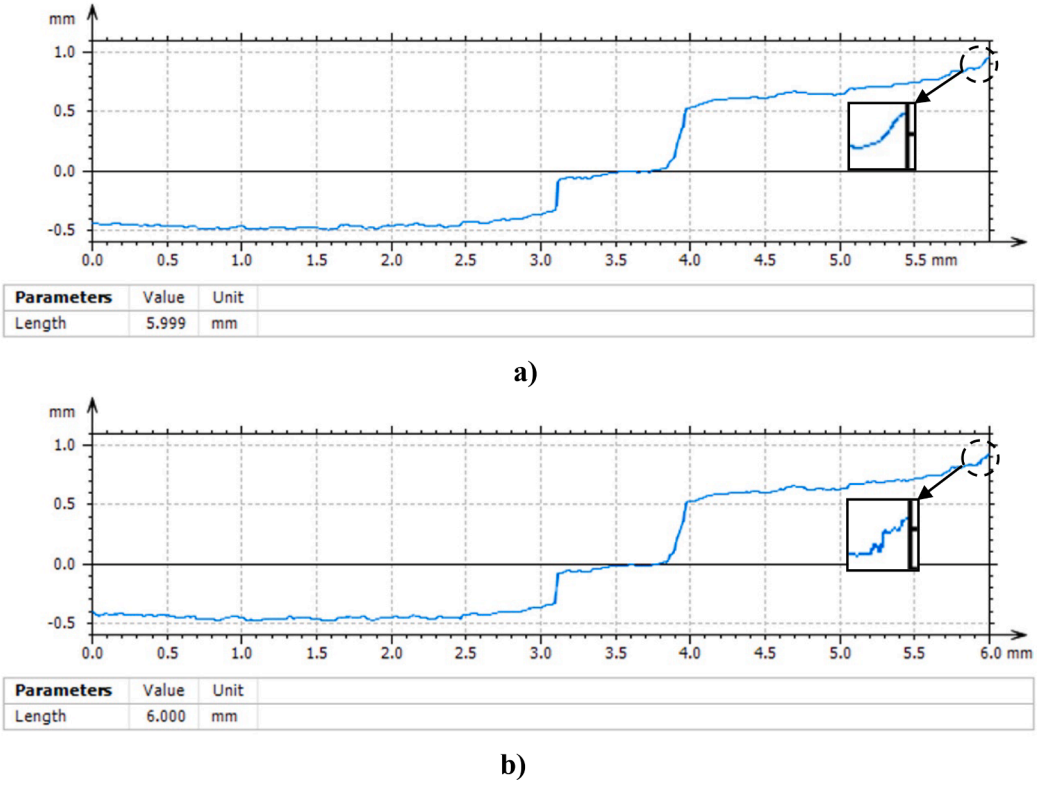

Fig. 9. Profiles extracted from entire bending-fatigued fracture surfaces (specimen no. 3) using focus variation microscopy (a) and confocal (b) methods.

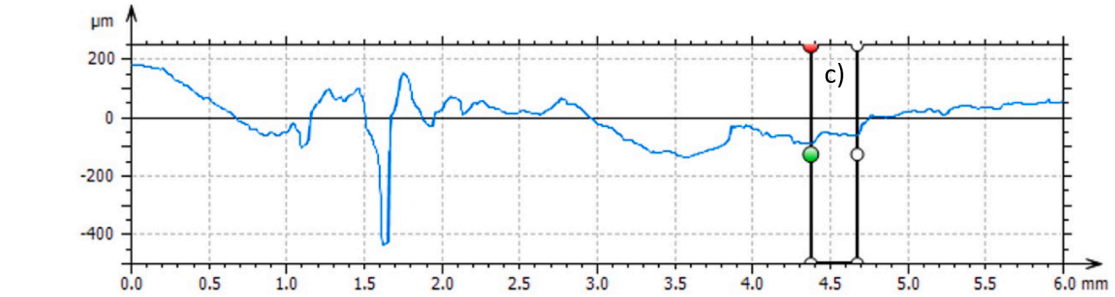

Parameters	Value	Unit
Length	6.001	mm

a)

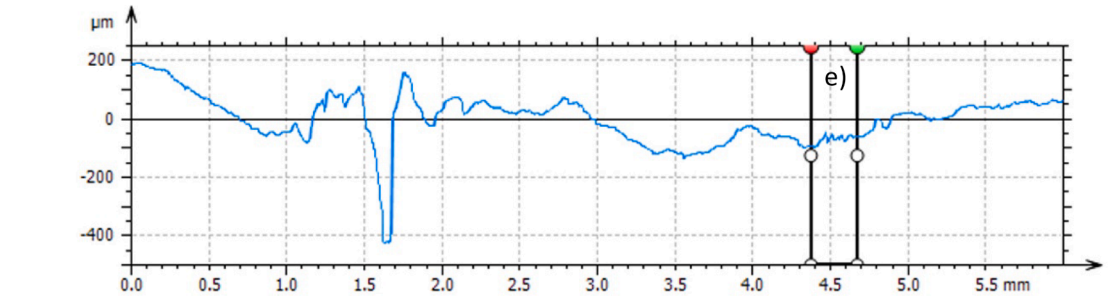

Parameters	Value	Unit
Length	5.999	mm

b)

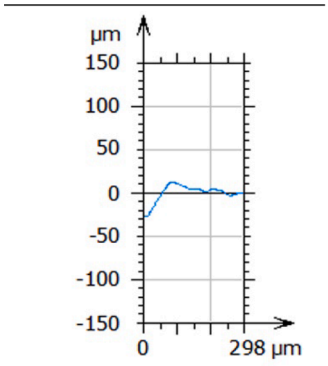

c)

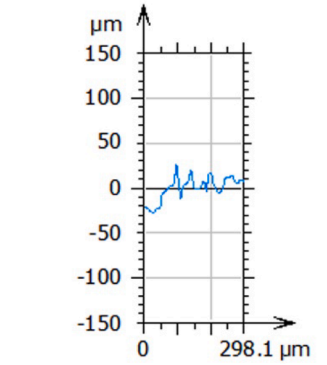

e)

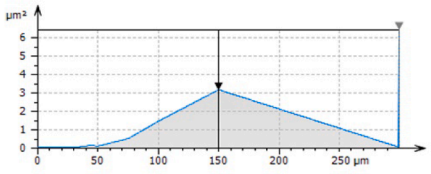

Information	
Zoom factor	x1
Number of iterations	1
Smoothing	None
Window function	Hann

Parameters	Value	Unit
Wavelength	149.9	µm
Magnitude	1.775	µm
Dominant wavelength	299.7	µm
Maximum magnitude	2.534	µm

d)

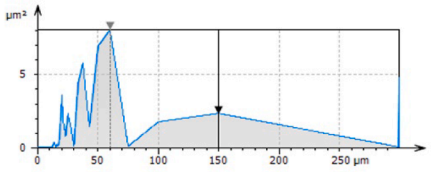

Information	
Zoom factor	x1
Number of iterations	1
Smoothing	None
Window function	Hann

Parameters	Value	Unit
Wavelength	149.7	µm
Magnitude	1.522	µm
Dominant wavelength	59.87	µm
Maximum magnitude	2.839	µm

f)

Fig. 10. Surface topography profiles extracted from entire bending-fatigued fracture (specimen no. 3) after measurement by focus variation microscopy (a) and confocal (b) equipment, their extracted noise-areas (c,e) and PSDs (d,f), respectively.

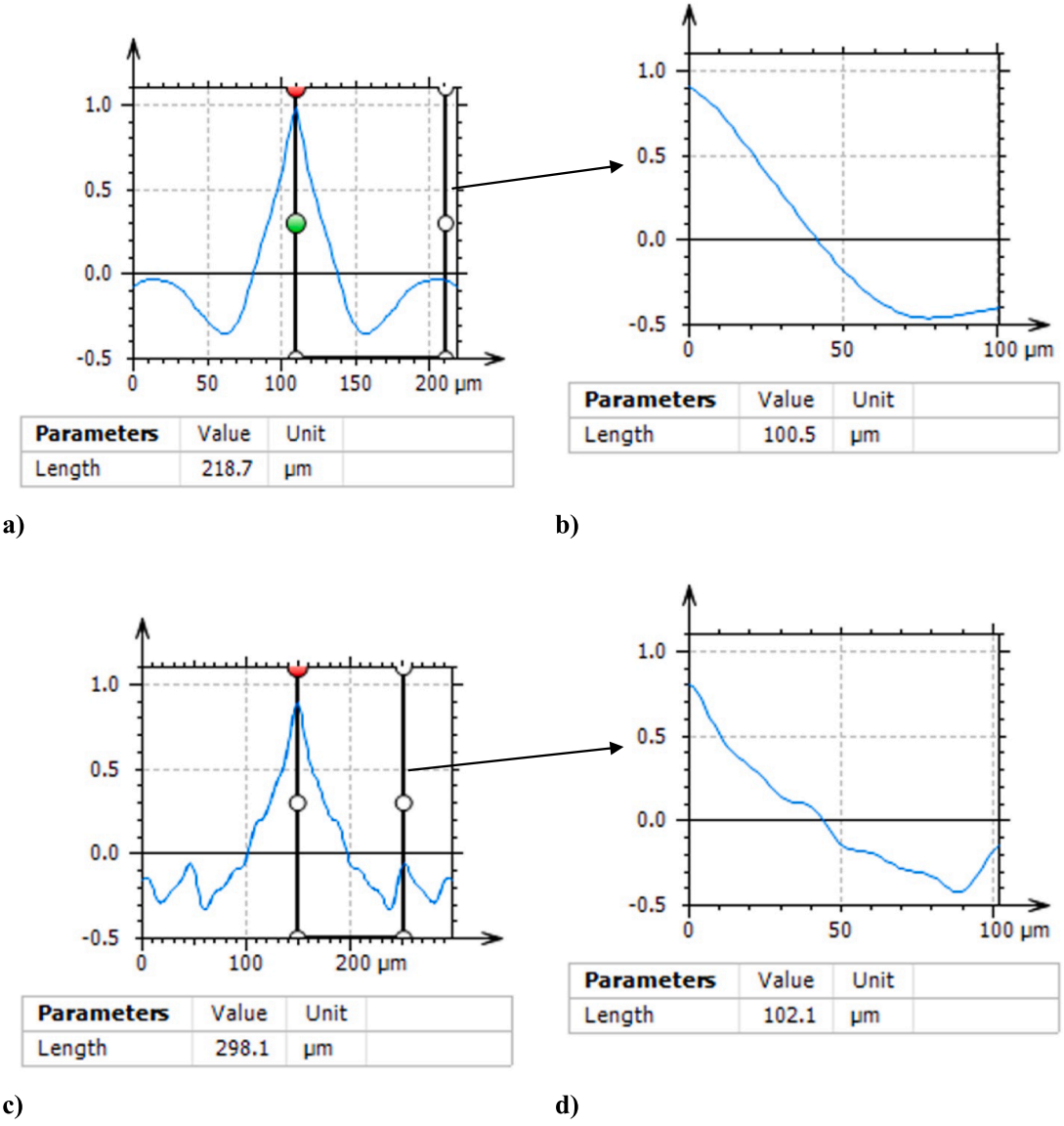

Fig. 11. The autocorrelation function (a,c) of extracted noise areas from profiles presented in Fig. 9c and 9e, respectively, and their enlarged centre parts (b,d). Data received for the focus variation microscopy (a,b) and confocal (c,d) measurements of specimen no. 3.

Some additional improvements in the detection of high-frequency components in the measured data can be derived from the analysis of the autocorrelation function (ACF). Fig. 11 presents such functions for the profiles studied in the previous figure (Fig. 10). The differences were observed for the shape of the function. Moreover, the level of the increased function value in the centre part also changed. It was observed that if data contained high-frequency components, the enlargement in the function value was greater than that of data without high-frequency features.

The presence of high-frequency data in the results of surface topography measurements was observed after the application of both types of instruments. The differences in the PSDs and ACFs functions are indicated in Fig. 12 for both focus variation microscopy (Fig. 12a) and confocal (Fig. 12b) methods. From that observation, high-frequency bandwidth filtration can be proposed for results received after the usage of both measuring techniques. After the elimination of non-measured and outlier points, the results of the reduction of the high-frequency noise were evaluated.

In the field of roughness studies, digital filters play a significant role. Numerous algorithms [61] and methodologies [62] have been proposed and refined for characterizing surface topography. Among these, digital filters [63], spline techniques [64], wavelet transforms and filters [65], morphological schemes based on envelope operations [66] and other advanced methods [67] have been widely recognized. ISO standards have also endorsed filters based on the Gaussian function [68], which are the most popular for roughness filtering. Additionally, many procedures are compared to conventional Gaussian filtering methods [69]. The Gaussian function filter, in particular, is essential as the S-filter for suppressing small-scale components in the raw measured surface topography data [70].

2.4. *Proposed procedure*

Fig. 13 presents the flow chart of the proposed procedure. The main procedure can be subdivided into two distinct components: data preprocessing and the process for mitigating high-frequency measurement errors.

In the data preparation phase, the first step was focused on the measurement of surfaces by two techniques: focus variation microscopy and confocal methods. Secondly, from the raw measured data, details were extracted to receive similar areas of study. Then, surfaces were levelled using the least-square plane (LSPL) method. In the subsequent

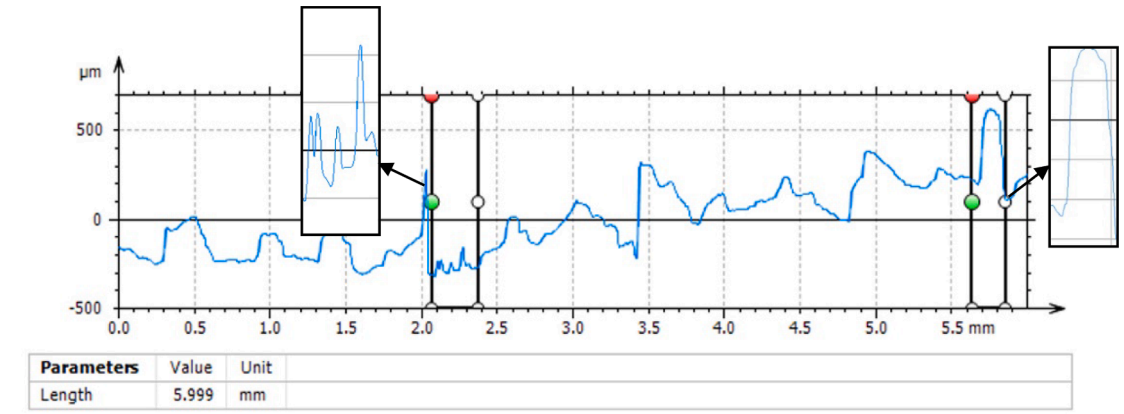

Parameters	Value	Unit
Length	5.999	mm

a)

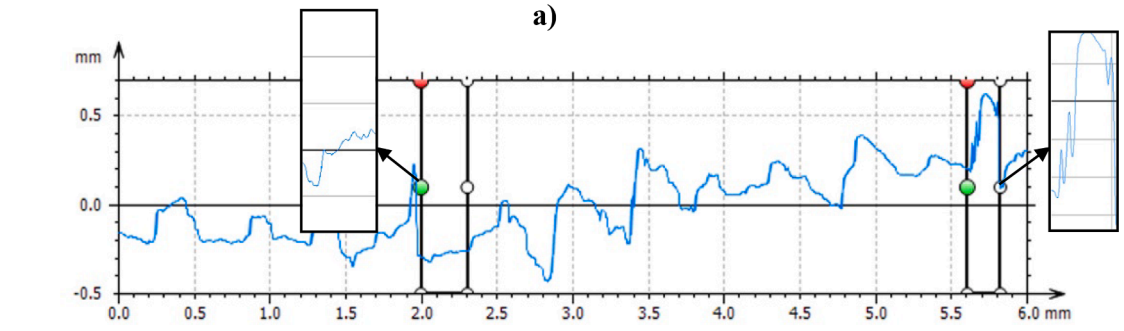

Parameters	Value	Unit
Length	6.001	mm

b)

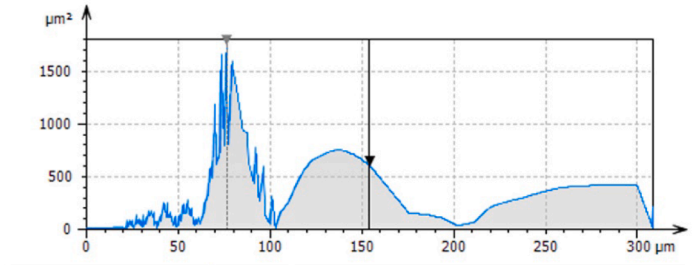

Parameters	Value	Unit
Dominant wavelength	76.24	µm
Maximum magnitude	41.74	µm

c)

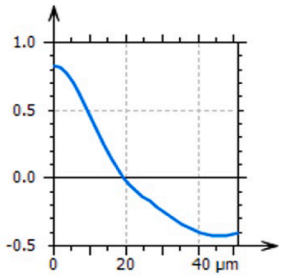

Parameters	Value	Unit
Length	51.14	µm

d)

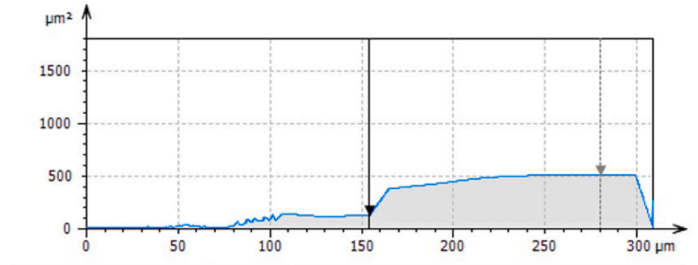

Parameters	Value	Unit
Dominant wavelength	280.4	µm
Maximum magnitude	22.35	µm

e)

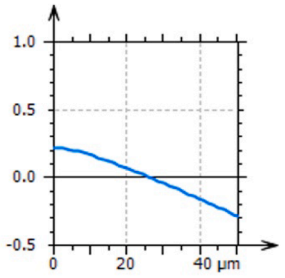

Parameters	Value	Unit
Length	50.57	µm

f)

Fig. 12. Profiles extracted from the entire bending-fatigued fracture surface (specimen no. 3) using focus variation microscopy (a) and confocal (b) methods with enlarged profile noise areas, their PSDs (c,e) and the centre parts of ACFs (d,f), respectively.

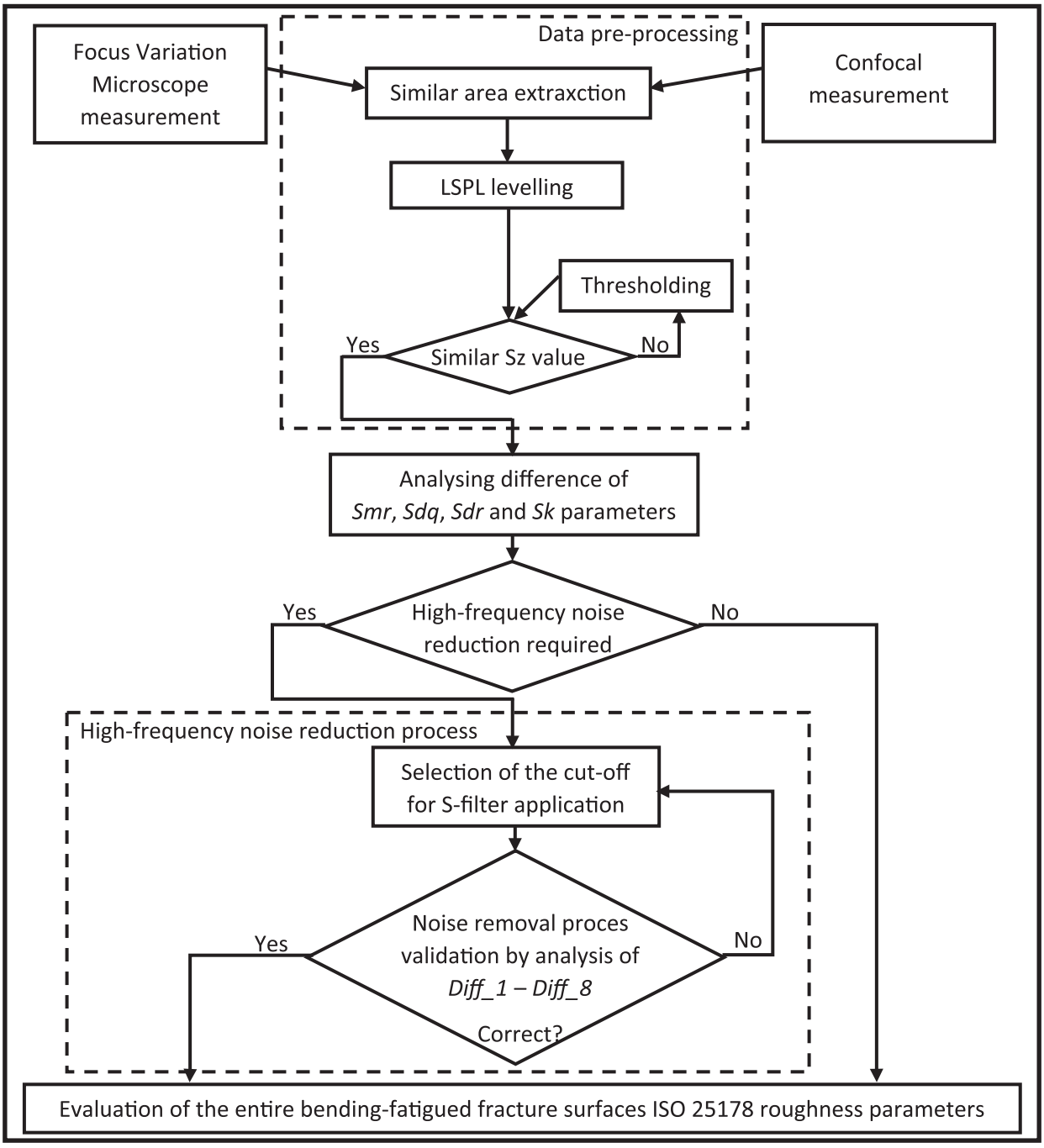

Fig. 13. The flow chart of the applied procedure.

pre-processing step, the maximum height of the surface (*Sz*) was compared for both measuring instruments. If the values were different, the thresholding technique was applied to harmonize the results. In such cases, outliers were eliminated using the thresholding technique.

The thresholding method used for the outlier removal is a common approach that operates on height data, making it a straightforward and effective method for segmenting surface topography data. However, it is important to note that a simple thresholding technique may not provide stable results when dealing with surfaces that contain stochastic elements, as this can lead to challenges in accurately characterising the number of defects and feature density [71].

When determining the appropriate thresholding cut value, it was observed that for random surfaces, the height difference between material ratios ranging from 0.13 to 99.87 % equals 6 standard deviations of surface amplitude [72]. In addition, it was also noted that for common types of surface topography, the material ratios fall within the range of 0.13 % to 99.87 %, designated for areal surface height, very similar to that of a profile [73].

In the subsequent step, the noise-sensitive ISO 25178 roughness parameters were assessed. An analysis of the surface topography of each specimen revealed that differences in noise-sensitive parameters were significantly higher than other ISO 25178 indicators. Based on this observation, it can be inferred that the variations in the obtained data can be attributed to the presence of high-frequency errors, indicating that the data from the first instrument may contain more high-frequency components compared to the data acquired from the second device.

After that, the noise-sensitive parameters (*Smr*, *Sdq*, *Sdr*, and *Sk*) were comprehensively analysed by applying a noise-suppression filter. If

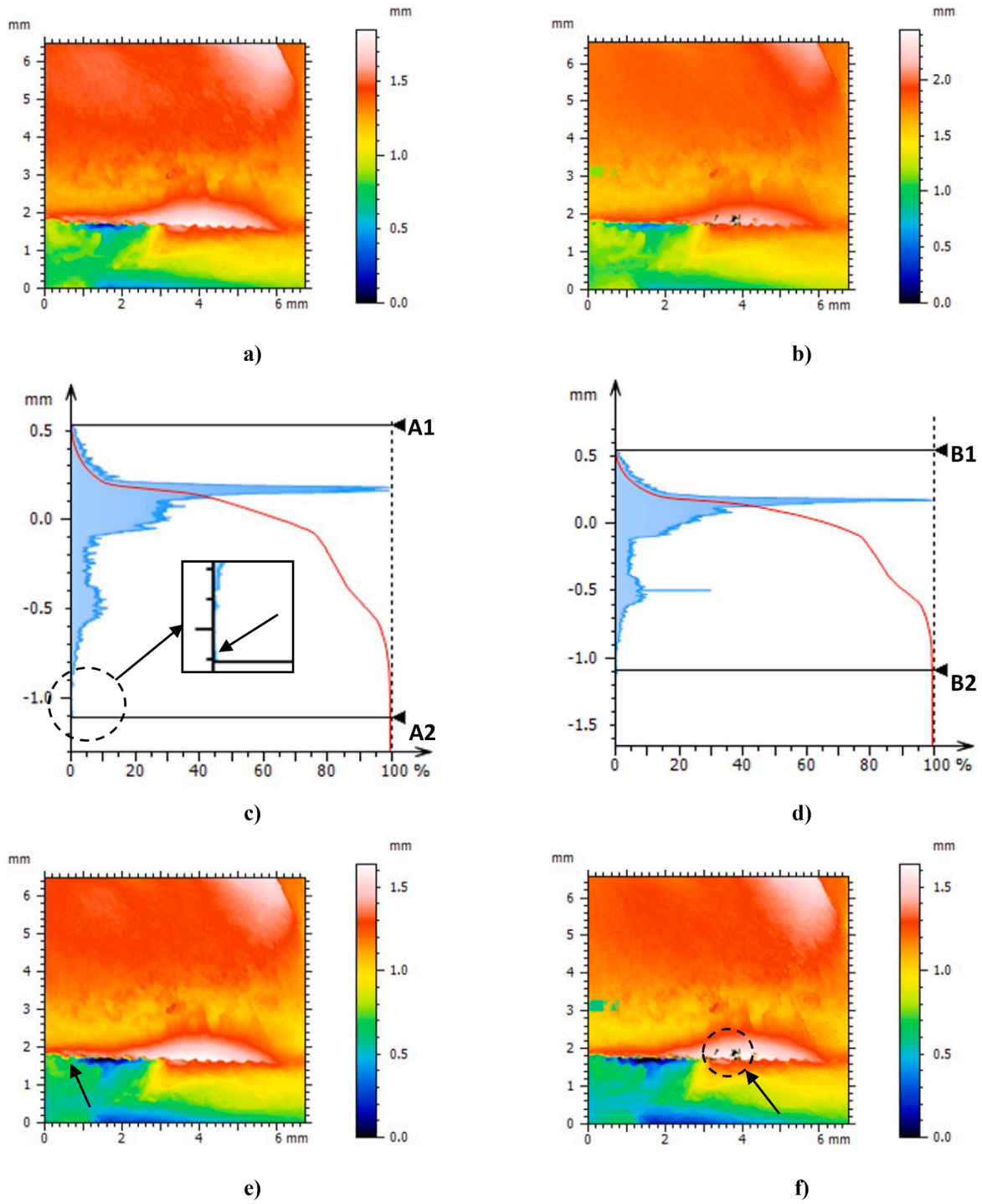

Fig. 14. Contour map plots of the entire bending-fatigued fracture surface (specimen no. 1) measured with focus variation microscopy (a) and confocal (b) technique, the method of selection of the thresholding value (c,d) and thresholded surface topography data (e,f).

there was a need to reduce high-frequency measurement noise, a procedure to select the cut-off value for the S-filter was employed. This selection was based on minimizing the differences in the ISO 25178 surface roughness parameters, expressed as *Diff_1 – Diff_8*.

Numerous digital filters are available for filtering high-frequency data from the raw measurements. In this study, the commonly used S-filter, available commercially, was used to assess its influence on both the noise removal process and the variation in ISO 25178 roughness parameters. The study did not designate other filters. Here, the main purpose was to introduce a procedure that incorporates the common roughness filtration scheme and offers guidance on reducing errors during data processing.

When selecting the cut-off value for the S-filter cut, the main aim was to minimize the differences in noise-sensitive parameters without affecting other ISO 25178 roughness indicators. In practical terms, digital filtering has an impact on both measured data and roughness parameters. The most promising approach in mitigating high-frequency noise is to minimize variations in noise-sensitive parameters while keeping the other indicators unaffected. Consequently, a comprehensive analysis of all of the proposed parameter variations (from *Diff_1* to

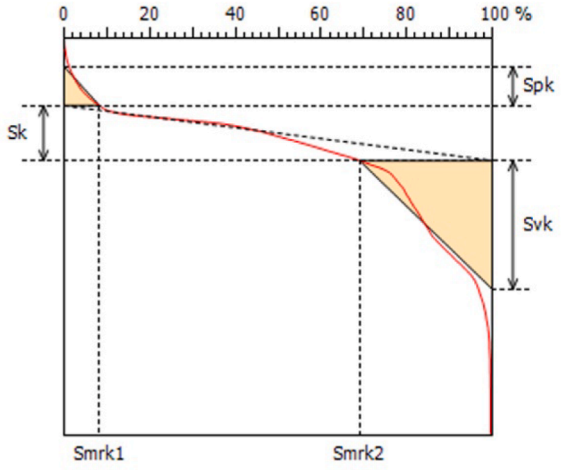

Information	
Filter settings	Unfiltered.

Parameters	Value	Unit
Sk	0.2549	mm
Spk	0.1810	mm
Svk	0.5975	mm
Smrk1	8.275	%
Smrk2	68.98	%

a)

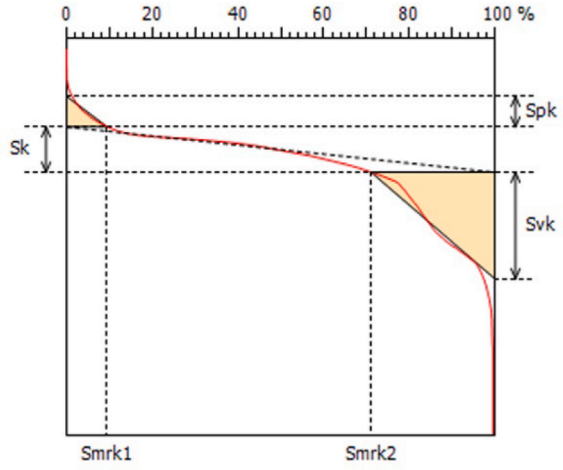

Information	
Filter settings	Unfiltered.

Parameters	Value	Unit
Sk	0.2784	mm
Spk	0.1880	mm
Svk	0.6553	mm
Smrk1	9.447	%
Smrk2	71.11	%

b)

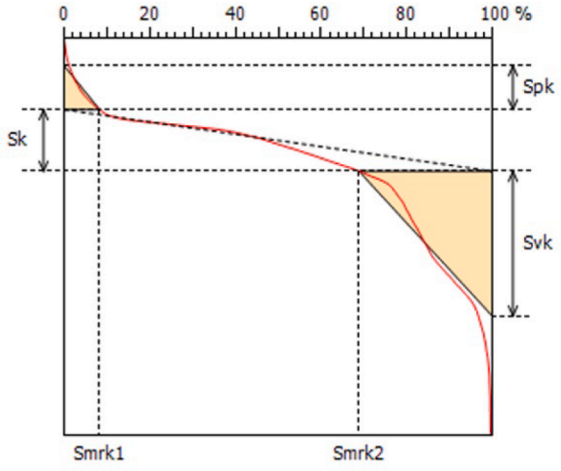

Information	
Filter settings	Unfiltered.

Parameters	Value	Unit
Sk	0.2539	mm
Spk	0.1811	mm
Svk	0.5966	mm
Smrk1	8.294	%
Smrk2	68.86	%

c)

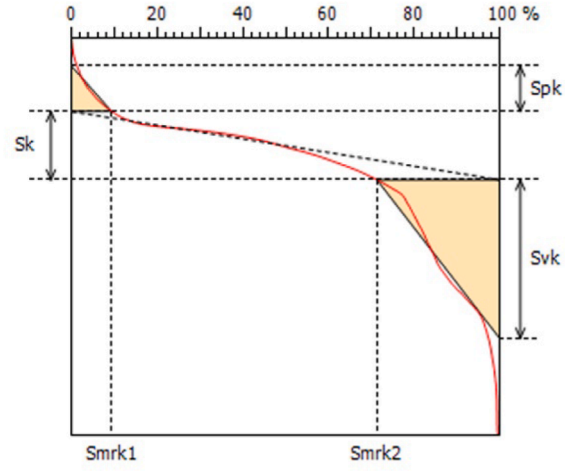

Information	
Filter settings	Unfiltered.

Parameters	Value	Unit
Sk	0.2814	mm
Spk	0.1873	mm
Svk	0.6534	mm
Smrk1	9.379	%
Smrk2	71.32	%

d)

Fig. 15. Material ratio curves of the entire bending-fatigued fracture surface (specimen no. 1) measured with focus variation microscopy (a) and confocal (b) technique, before (a,b) and after (c,d) application of the thresholding technique.

Table 4
The relative differences (expressed in %) of ISO 25178 roughness parameters for the entire bending-fatigued fracture surfaces (specimen no. 1) measured with a focus variation microscope and confocal methods.

Groups and parameters		Units	*Diff_1*	*Diff_2*	*Diff_3*	*Diff_4*
Height parameters	*Sq*	mm	−6.68	0.00	0.64	−5.99
	Ssk		−7.12	0.00	4.98	−1.78
	Sku		−14.78	0.00	11.28	−1.83
	Sp	mm	−44.25	3.50	30.80	−3.43
	Sv	mm	−27.38	14.62	34.06	1.62
	Sz	mm	−32.32	11.37	33.02	0.00
	Sa	mm	−5.95	0.00	0.24	−5.70
Functional parameters	*Smr*	%	39.77	−162818.19	−361860.33	−33.82
	Smc	mm	−11.67	0.05	0.17	−11.53
Spatial parameters	*Sal*	mm	−8.26	0.00	0.00	−8.26
	Std	°	98.03	0.00	0.03	98.03
Hybrid parameters	*Sdq*		−520.46	0.64	12.35	−447.33
	Sdr	%	−545.75	0.10	4.10	−519.89
Functional parameters (volume)	*Vm*	mm^3/mm^2	−0.72	0.00	0.02	−0.70
	Vv	mm^3/mm^2	−11.22	0.00	0.16	−11.04
	Vmp	mm^3/mm^2	−0.72	0.00	0.02	−0.70
	Vmc	mm^3/mm^2	−4.36	0.00	0.00	−4.36
	Vvc	mm^3/mm^2	−12.06	0.00	0.00	−12.06
	Vvv	mm^3/mm^2	−8.83	0.00	0.60	−8.18
Functional parameters (stratified surfaces)	*Sk*	mm	−9.22	0.39	−1.08	−10.83
	Spk	mm	−3.87	−0.06	0.37	−3.42
	Svk	mm	−9.67	0.15	0.29	−9.52
	Smr1	%	−14.16	−0.23	0.72	−13.08
	Smr2	%	−3.09	0.17	−0.30	−3.57

Table 5
The relative differences (expressed in %) of ISO 25178 roughness surface parameters for the entire bending-fatigued fracture surfaces (specimen no. 3) measured with a focus variation microscope and confocal methods.

Group of parameters	Parameters	Units	*Diff_5*	*Diff_6*	*Diff_7*	*Diff_8*
Height parameters	*Sq*	mm	3.44	0.03	0.03	3.44
	Ssk		−1.07	−0.05	−0.14	−1.16
	Sku		−1.35	−0.03	−0.09	−1.41
	Sp	mm	2.58	0.29	1.18	3.45
	Sv	mm	−3.28	0.14	0.00	−3.43
	Sz	mm	0.56	0.25	0.75	1.06
	Sa	mm	4.06	0.04	0.04	4.06
Functional parameters	*Smr*	%	−100.46	−59.17	38.05	21.97
	Smc	mm	3.17	0.02	0.02	3.17
	Sxp	mm	2.58	0.06	0.15	2.66
Spatial parameters	*Sal*	mm	0.00	0.00	0.00	0.00
	Std	°	0.17	0.00	0.11	0.28
Hybrid parameters	*Sdq*		−80.32	41.94	59.87	−24.64
	Sdr	%	−168.77	15.27	55.34	−41.66
Functional parameters (volume)	*Vm*	mm^3/mm^2	2.12	−0.06	0.00	2.18
	Vv	mm^3/mm^2	3.15	0.02	0.02	3.15
	Vmp	mm^3/mm^2	2.12	−0.06	0.00	2.18
	Vmc	mm^3/mm^2	3.92	0.03	0.00	3.89
	Vvc	mm^3/mm^2	3.23	0.02	0.00	3.21
	Vvv	mm^3/mm^2	0.14	0.07	0.28	0.35
Functional parameters (stratified surfaces)	*Sk*	mm	8.28	0.14	0.06	8.20
	Spk	mm	−0.70	−0.13	−0.07	−0.63
	Svk	mm	−4.88	1.04	2.00	−3.86
	Smr1	%	−1.87	0.00	0.05	−1.82
	Smr2	%	3.64	0.03	0.04	3.65

Diff_8) becomes crucial in validating the suitability of the procedure.

3. Results and discussions

3.1. Application of compensation techniques for the measurement data comparison with outlier removal

The reduction of differences in the results of focus variation microscopy and confocal measurements was found mainly in the presence of non-measured points, outliers and high-frequency measurement errors. Generally, the locations of occurrence of the above three types of errors were different, depending on the technique of measurement.

Omitting the distortion in the removal of the spikes with the application of digital filtering, including morphological (with upper and lower envelope) and robust modifications, the thresholding technique was used. The main limitation in the correct usage of the threshold method is the selection of the cut-off value. False definitions of the threshold value can cause the removal of sufficient features for the surface properties characterisation and, especially, an increase in errors of the calculated ISO 25178 roughness parameters.

Fig. 14 proposes a methodology for the selection of the thresholding bandwidth. When comparing the results of measurement using the focus variation microscopy technique and the confocal method, the minimisation in differences of ISO 25178 parameters was inquired. Firstly, the difference in the maximum height of the surface, calculated as the *Sz* parameter, was studied. The variations in the maximum height of the

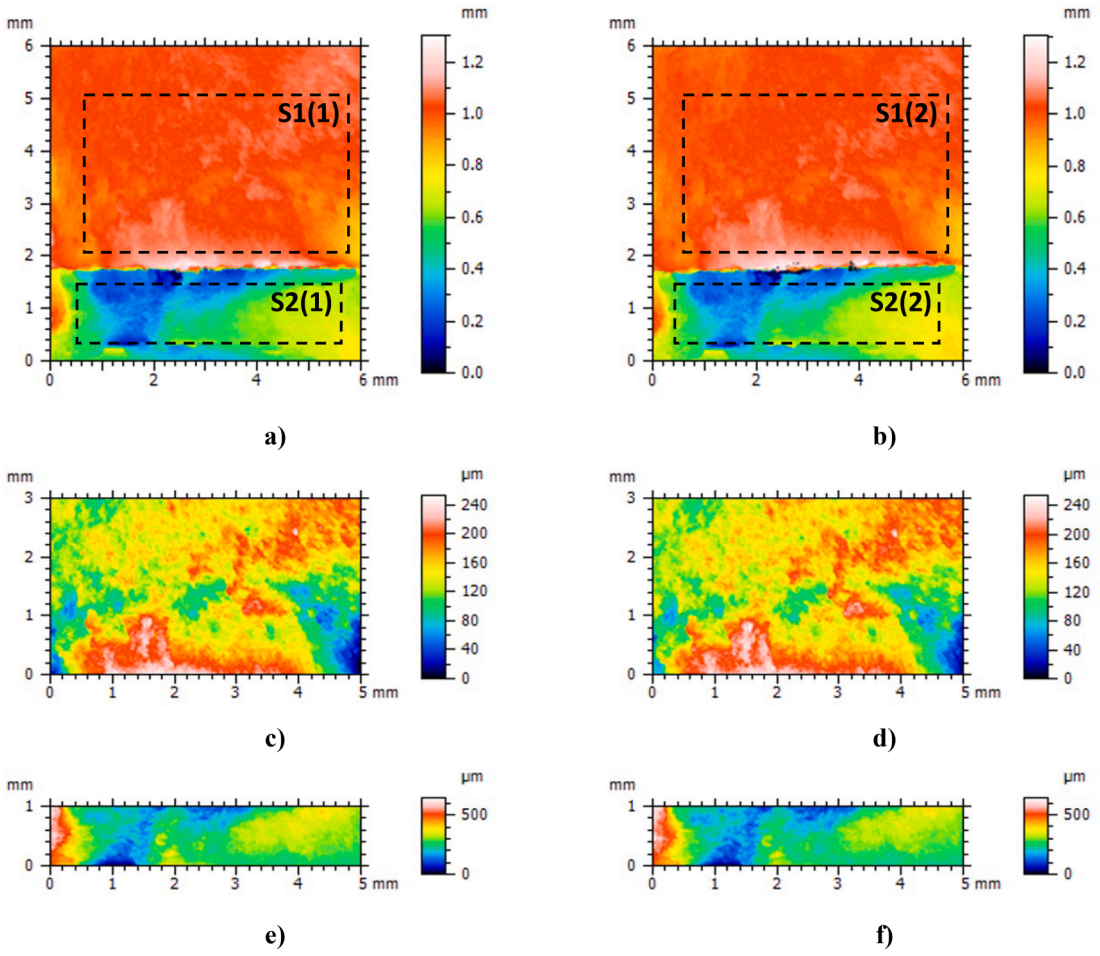

Fig. 16. Contour map plots of entire bending-fatigued fracture surface topography (specimen no. 2) measured with focus variation microscopy (a) and confocal (b) methods after outlier removal by thresholding technique, 0.13 %-99.87 %, and suppression of high-frequency errors with an application of S-filter, cut-off = 0.008 mm, and the subsurfaces S1(1) (c), S1(2) (d), S2(1) (e) and S2(2) (f) extracted from different areas of detail, respectively.

surface measured with focus variation microscope and confocal methods are visible in the isometric view of the surface (Fig. 14a and Fig. 14b).

To minimise the variance of the *Sz* parameter, different thresholding values were required, defined as A1 and A2 for the focus variation microscopy measurements, and B1 and B2 for the confocal technique (Fig. 14c and Fig. 14d), respectively. The precision of the selection of the thresholding bandwidth was crucial in retaining all of the required surface features. In Fig. 14c, examples of the enlarged limit value selection are presented and indicated by the arrow. For different surfaces, especially after various entire bending-fatigued fractures, the value can vary significantly. Receiving the similarity in the maximum height (*Sz*) of the surface, some measurement differences in the focus variation microscope and confocal methods can be visible more directly (identified by arrows in Fig. 14e and Fig. 14f).

The suppression of the outliers by the thresholding technique did not change the parameters of material ratio curves significantly. As presented in Fig. 15, the differences for both types of measurement were smaller than 1 %, calculating the data before and after the application of the thresholding method. For a more comprehensive ISO 25178 surface roughness comparison, the four differences in values of parameters from various groups were investigated, see Table 4. The first difference (*Diff_1*) indicated the variation in parameters received by the two measurement methods. The second (*Diff_2*) and third (*Diff_3*) variations presented deviations in parameters obtained before and after the usage of the thresholding approach for the focus variation microscope and confocal measurements, respectively. The last variation (*Diff_4*) was determined for data after thresholding, computing the differences between focus variation microscopy and confocal measurements.

Analysing the *Diff_1* values, it is clear that the greatest differences were obtained for the selected amplitude (height), functional, spatial and hybrid parameters. For hybrid *Sdq* and *Sdr* parameters, the differences were enormous, over 500 %. The maximum height of the surface, determined using *Sz* parameters varies about 30 %. Considering the differences *Diff_2* and *Diff_3*, thresholding processing of the data did not modify the ISO 25178 parameters significantly (except the maximum peak height *Sp*, maximum valley depth *Sv*, *Sz* and *Smr*), usually under 1 % of the deviation. This can be crucial since the thresholding approach influences the parameters similarly for both measuring methods. The highly encouraging results were collected for the difference *Diff_4*. All variations in the values of the height parameters, especially for *Sp* (from 44.25 % to 3.43 %), *Sv* (from 27.38 % to 1.62 %) and *Sz* (from 32.32 % to 0 %), were reduced significantly by comparing both measuring techniques. The differences for functional, spatial and hybrid parameters were not reduced substantially, and the variations were negligible. In addition, it can be concluded that the thresholding technique reflects the amplitude of data and, simultaneously, the amplitude parameters.

3.2. *Improving proposed methods with the reduction in differences of ISO 25178 parameters with suppression of high-frequency measurement errors*

One of the major issues in surface metrology when analysing surface roughness is the compensation of high-frequency measurement errors.

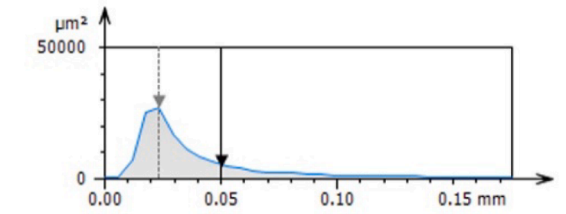

Information	
Zoom factor	x32
Smoothing	None
Window function	None

Parameters	Value	Unit
Wavelength	0.05254	mm
Magnitude	65.74	µm
Dominant wavelength	0.02335	mm
Maximum magnitude	164.6	µm

a)

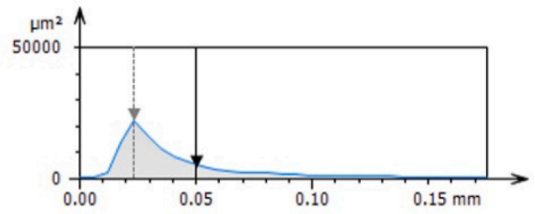

Information	
Zoom factor	x32
Smoothing	None
Window function	None

Parameters	Value	Unit
Wavelength	0.05254	mm
Magnitude	64.86	µm
Dominant wavelength	0.02335	mm
Maximum magnitude	148.7	µm

b)

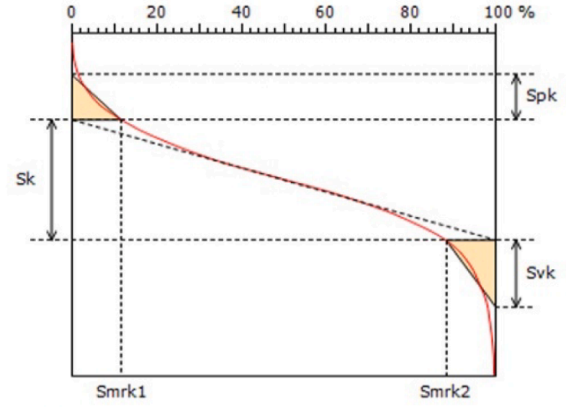

Information	
Filter settings	Unfiltered.

Parameters	Value	Unit
Sk	88.65	µm
Spk	33.06	µm
Svk	49.22	µm
Smrk1	11.54	%
Smrk2	88.27	%

c)

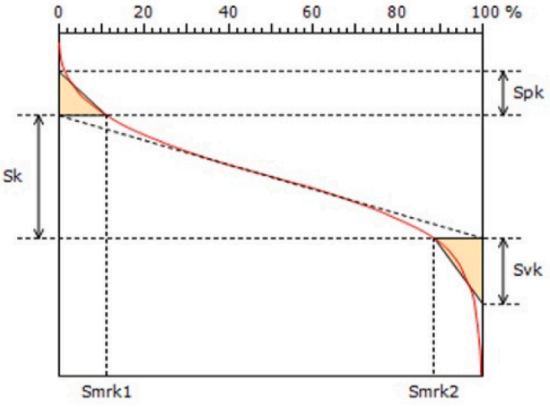

Information	
Filter settings	Unfiltered.

Parameters	Value	Unit
Sk	88.03	µm
Spk	31.57	µm
Svk	46.99	µm
Smrk1	11.25	%
Smrk2	88.59	%

d)

Fig. 17. The PSDs (a,b) and material ratio curves (c,d) of the S1(1) (a) and S1(2) (b) details.

The comparison of focus variation microscopy and confocal methods for measurement of entire bending-fatigued fracture surfaces, when the non-measured and outlier points were compensated, demonstrated that the differences were obtained due to the presence of high-frequency data. Except for the isometric view of the surface and profile explorations, as previously presented in Figs. 5 and 6, the differences were also detected in the values of calculated ISO 25178 roughness parameters, see Fig. 7. The substantial differences in the high-frequency noise-sensitive parameters indicated the occurrence of high-frequency data in the results of measurement obtained through both techniques. The occurrence of the high-frequency components in the measured data was improved by PSD and ACF characterisation as well.

In Table 5, the four relative differences, expressed in percentage, were presented for ISO 25178 surface roughness parameters. The first parameter difference (*Diff_5*) was calculated for entire bending-fatigued fracture surfaces measured with focus variation microscopy and confocal methods. Those data were pre-processed by fulfilling the NMPs and removal of outliers, as extensively presented in previous studies. The further differences (*Diff_6*, *Diff_7* and *Diff_8*) are related to data after the application of the S-filter with a cut-off equal to 0.015 mm. The second (*Diff_6*) and third (*Diff_7*) differences compared the parameters measured by the focus variation microscope and confocal methods, respectively, before and after the usage of the S-filter. This correlation presented how values of roughness parameters were changed with digital filtration for each type of measuring technique. The last difference (*Diff_8*) denoted the variation in ISO 25178 topography parameters after S-filtration and was determined between the focus variation microscope and confocal measurements.

The most sensitive parameters to high-frequency errors (*Smr*, *Sdq*, *Sdr* and *Sk*) were differentiated between various measurement techniques. *Diff_5* varied between 5 % (*Sk* parameter) and 180 % (*Sdr* indicator). Those variations were reduced when the S-filter was applied.

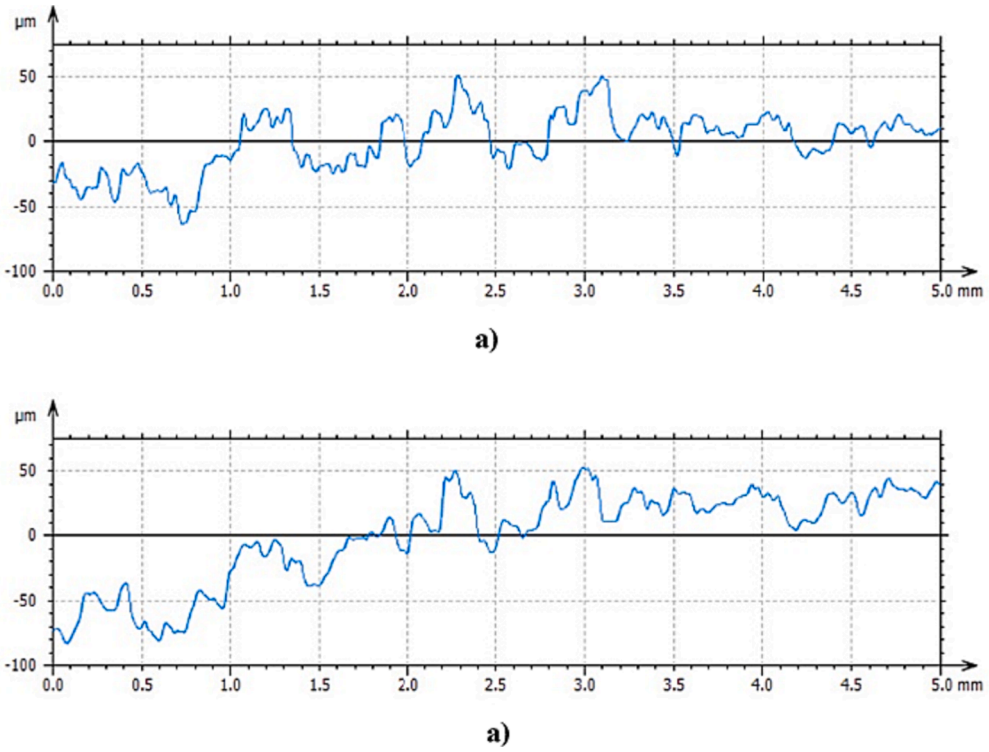

Fig. 18. Profiles from the entire bending-fatigued fracture surface topography (specimen no. 2) measured with focus variation microscopy (a) and confocal (b) methods, after outlier and high-frequency measurement noise removal by thresholding and S-filter techniques, respectively.

Considering the FVM measurement, the disparities for the surface before and after S–filtration were reduced to around 60 % for *Smr*, 40 % for *Sdq*, 15 % for *Sdr* and 0.14 % for *Sk* parameters. On the contrary, for the confocal method, the S-filter diminished the distortion of *Smr*, *Sdq*, *Sdr* and *Sk* parameters to around 40 %, 60 %, 55 % and 0.07 %, respectively. An interesting outcome related to the application of a commercial S-filter was that this digital processing did not significantly modify the values of parameters classified as those non-sensitive to the presence of the high-frequency errors (all presented except the *Smr*, *Sdq*, *Sdr* and *Sk* parameters). In general, those differences were smaller than 0.5 %, as suggested by the values of *Diff_6* and *Diff_7* in Table 5.

However, the particularly promising outcome is that the variations in the high-frequency noise-sensitive parameters, calculated between two types of measurements, are reduced when the S-filtration is implemented, as demonstrated by the values of *Diff_8* in Table 5. The deviation of the functional parameter Smr decreased from around 100 % to 20 %, while for the hybrid parameters Sdq and Sdr, the deviation decreased from approximately 80 % and 170 % to 25 % and 40 %, respectively. As the limitation, the diminishment of the functional parameter *Sk* was negligible, nevertheless, this parameter is crucial in the characterisation of stratified surfaces. Consequently, the reduction of the parameters highly susceptible to the occurrence of high-frequency error was obtained.

Additionally, Fig. 16 shows the isometric views of the entire bending-fatigued fracture surface topography measured by both methods. From surface data (Fig. 16a and Fig. 16b), details from various areas (Fig. 16c-f) were extracted. The similarity of surface views for both the whole measured surface and enlarged areas was also highlighted. After separating the surface areas, the differences in the dominant wavelengths were negligible or did not exist (Fig. 17) when the PSDs were investigated. It was found that the maximum magnitude was greater for the focus variation microscope measurements. The differences in the material ratio curve parameters of the enlarged detail were also reduced. Considering the profile data (Fig. 18), the areas of outliers and high-frequency errors were also not recognized.

Errors in calculating the *Sk* (material ratio curves) roughness parameters can be crucial in the bending-fatigued fracture surface topography analysis because it is linearly dependent on the strain amplitude and logarithmically dependent on the fatigue life N_f, as presented by Macek et al. in [74]. Consequently, the value of the further amplitude parameter, e.g. the arithmetical mean height *Sa*, can be related to the fractal dimension D_f through a linear function. Generally, it was proved that, taking into account ISO 25178 surface roughness parameters, it was possible to estimate the type of loading and to some extent the number of cycles to failure N_f, at which the analysed element failed [27].

The presented method for comparison of the results of entire bending-fatigued fracture surface roughness measurements obtained with a focus variation microscope and confocal techniques is valuable in the reduction of measurement errors, like non-measured points, outliers or high-frequency measurement noise.

The differences in the presence of high-frequency noise data in the results of surface topography measurements using focus variation and confocal techniques can be justified by the nature of each of the method. In focus variation microscopy, when data is collected by acquiring images at different focal points and calculating changes in focal length, the high-frequency components can be categorized as specific results. Conversely, when measuring with confocal instruments, which employs very high lateral resolution, the high-frequency data is considered undesirable and is automatically excluded from the final results of the surface topography measurement process. In an overall comparison, confocal technology holds an advantage is detecting high-frequency noise due to its superior spatial resolution, setting it apart from the focus variation technique.

However, by improving the similarity of measurement carried out with various techniques, the errors related to the measurement process can be reduced. It was found that the presence of outliers can significantly affect the confocal results. Nevertheless, the thresholding technique can be proposed for both types of data computation.

Reduction of high-frequency measurement noise is required for both measuring methods, for this type of error the commercially available

S–filter can be suitable for improving the data similarity. However, for further studies, the proposed procedure must be thoroughly investigated for the selection of a type of filter (compared to other available solutions in commercial software) and its bandwidth (cut-off) characteristics.

4. Conclusions

Based on all studies presented above, the following conclusions can be drawn:

- The errors received by various optical methods, including focus variation microscopy and confocal techniques, can be reduced by comparing the measurement differences. For both types of measuring instruments, the non-measured points, outliers (spikes) and high-frequency noise were detected. The differences in the compensations of those errors can vary the values of the ISO 25178 surface roughness parameters significantly.
- The variations in the height parameters were mainly verified with the outliers identifications. The removal of the individual peaks reduced the differences in the amplitude parameters by under 5 %, excluding the core roughness *Sk*, where variances between the measuring techniques were up to 10 %. Similar variations for height parameters were obtained after high-frequency measurement noise suppression.
- The application of the noise reduction procedure (S-filter with bandwidth 8 μm) modified the ISO 25178 parameters. The most relevant differences were obtained for high-frequency noise-sensitive parameters: root mean square gradient *Sdq*, developed interfacial areal ratio *Sdr*, and areal material ratio *Smr*. The values of reduced core roughness *Sk* were not improved, and the differences between the two measuring techniques were not appropriately minimised.
- The method for reduction of measurement errors, including filling-in of non-measured points, removal of outliers and reduction of high-frequency measurement errors, can be selected with a minimisation of the differences between the results of the two methods of measurement. For each type of those three measuring errors, sensitive parameters must be extensively studied. When the variations of the error-sensitive parameters are reduced and, respectively, the other ISO 25178 indicators (especially those influencing the fatigue characteristics) are not distorted, the approach can be classified as suitable for compensating the measurement errors in the analysis of selected types of surfaces.

CRediT authorship contribution statement

Przemysław Podulka: Conceptualization, Methodology, Software, Validation, Formal analysis, Writing – original draft, Writing – review & editing, Visualization. **Wojciech Macek:** Conceptualization, Methodology, Software, Validation, Formal analysis, Writing – original draft, Writing – review & editing, Visualization. **Dariusz Rozumek:** Conceptualization, Investigation, Supervision. **Krzysztof Żak:** Software, Investigation, Supervision. **Ricardo Branco:** Validation, Writing – review & editing, Supervision.

Declaration of Competing Interest

The authors declare that they have no known competing financial interests or personal relationships that could have appeared to influence the work reported in this paper.

Data availability

Data will be made available on request.

Acknowledgement

This research is sponsored by national funds through FCT – Fundação para a Ciência e a Tecnologia, under the project UIDB/00285/2020 and LA/P/0112/2020.

References

[1] A. Rosenkranz, M. Marian, Combining surface textures and MXene coatings—towards enhanced wear-resistance and durability, Surf. Topogr.: Metrol. Prop. 10 (2022), 033001, https://doi.org/10.1088/2051-672X/ac7f4a.
[2] M. Padhan, U. Marathe, J. Bijwe, Surface topography modification, Film transfer and Wear mechanism for fibre reinforced polymer composites—An Overview, Surf. Topogr. Metrol. Prop. 8 (2020), 043002, https://doi.org/10.1088/2051-672X/abbcb6.
[3] M.L. Magri, A.E. Diniz, S.T. Button, Influence of surface topography on the wear of hot forging dies, Int J Adv Manuf Technol 65 (2013) 459–471, https://doi.org/10.1007/s00170-012-4185-1.
[4] J.M. Vázquez, J. Salguero, I. Del Sol, Texturing design of WC-Co through laser parameter selection to improve lubricant retention ability of cutting tools, Int. J. Refract. Met. h. 107 (2022), 105880, https://doi.org/10.1016/j.ijrmhm.2022.105880.
[5] R.W. Maruda, G.M. Krolczyk, S. Wojciechowski, B. Powalka, S. Klos, N. Szczotkarz, M. Matuszak, N. Khanna, Evaluation of turning with different cooling-lubricating techniques in terms of surface integrity and tribologic properties, Tribol. Int. 148 (2020), 106334, https://doi.org/10.1016/j.triboint.2020.106334.
[6] C.F. Yao, D.X. Wu, Q.C. Jin, X.C. Huang, J.X. Ren, D.H. Zhang, Influence of high-speed milling parameter on 3D surface topography and fatigue behavior of TB6 titanium alloy, T Nonferr. Metal. Soc. 23 (3) (2013) 650–660, https://doi.org/10.1016/S1003-6326(13)62512-1.
[7] O.V. Zakharov, A.V. Kochetkov, Minimization of the systematic error in centerless measurement of the roundness of parts, Meas. Tech. 58 (2016) 1317–1321, https://doi.org/10.1007/s11018-016-0892-6.
[8] P. Lu, R.J.K. Wood, Tribological performance of surface texturing in mechanical applications—a review, Surf. Topogr.: Metrol. Prop. 8 (2020), 043001, https://doi.org/10.1088/2051-672X/abb6d0.
[9] H.A. Abdel-Aal, Functional surfaces for tribological applications: inspiration and design, Surf. Topogr.: Metrol. Prop. 4 (2016), 043001, https://doi.org/10.1088/2051-672X/4/4/043001.
[10] G. Shen, F. Fang, C. Kang, Tribological performance of bioimplants: A comprehensive review, Nanotechnol. Precis. Eng. 1 (2018) 107–122, https://doi.org/10.13494/j.npe.20180003.
[11] M. Vishnoi, P. Kumar, M.Q. Qasim, Surface texturing techniques to enhance tribological performance: A review, Surf. Interfaces 27 (2021), 101463, https://doi.org/10.1016/j.surfin.2021.101463.
[12] B. Mao, A. Siddaiah, Y. Liao, P.L. Menezes, Laser surface texturing and related techniques for enhancing tribological performance of engineering materials: A review, J. Manuf. Process. 53 (2020) 153–173, https://doi.org/10.1016/j.jmapro.2020.02.009.
[13] Y.R. Jeng, C.C. Gao, Changes of Surface Topography during Wear for Surfaces with Different Height Distributions, Tribol. t. 43 (2000) 749–757, https://doi.org/10.1080/10402000008982404.
[14] T.D.B. Jacobs, L. Pastewka, Surface topography as a material parameter, MRS Bull. 47 (2022) 1205–1210, https://doi.org/10.1557/s43577-022-00465-5.
[15] R.S. Zhou, Surface Topography and Fatigue Life of Rolling Contact Bearing, Tribol. t. 36 (1993) 329–340, https://doi.org/10.1080/10402009308983167.
[16] W. Macek, Ł. Pejkowski, R. Branco, R.M. Nejad, K. Żak, Fatigue fracture surface metrology of thin-walled tubular austenitic steel specimens after asynchronous loadings, Eng. Fail. Anal. 138 (2022), 106354, https://doi.org/10.1016/j.engfailanal.2022.106354.
[17] J.F. Garcias, R.F. Martins, R. Branco, Z. Marciniak, W. Macek, C. Pereira, C. Santos, Quasistatic and Fatigue Behavior of an AISI H13 Steel Obtained by Additive Manufacturing and Conventional Method, Fatigue Fract. Eng. Mater. Struct. 44 (2021) 3384–3398, https://doi.org/10.1111/ffe.13565.
[18] K. Żak, W. Grzesik, Metrological aspects of surface topographies produced by different machining operations regarding their potential functionality, Metrol. Meas. Syst. (2017) 24, https://doi.org/10.1515/mms-2017-0027.
[19] T. Kobayashi, D.A. Shockey, Fracture surface topography analysis (FRASTA)—Development, accomplishments, and future applications, Eng. Fract. Mech. 77 (12) (2010) 2370–2384, https://doi.org/10.1016/j.engfracmech.2010.05.016.
[20] L. Molent, A. Spagnoli, A. Carpinteri, R. Jones, Using the lead crack concept and fractal geometry for fatigue lifing of metallic structural components, Int. J. Fatigue 102 (2017) 214–220, https://doi.org/10.1016/j.ijfatigue.2017.04.001.
[21] W. Macek, Z. Marciniak, R. Branco, D. Rozumek, G.M. Królczyk, A fractographic study exploring the fracture surface topography of S355J2 steel after pseudo-random bending-torsion fatigue tests, Measurement 178 (2021), 109443, https://doi.org/10.1016/j.measurement.2021.109443.
[22] D. Sampath, R. Akid, R. Morana, Estimation of crack initiation stress and local fracture toughness of Ni-alloys 945X (UNS N09946) and 718 (UNS N07718) under hydrogen environment via fracture surface topography analysis, Eng. Fract. Mech. 191 (2018) 324–343, https://doi.org/10.1016/j.engfracmech.2017.12.010.
[23] A. Carpinteri, A. Spagnoli, S. Vantadori, An approach to size effect in fatigue of metals using fractal theories, Fatigue Fract. Eng. Mater. Struct. 25 (2002) 619–627, https://doi.org/10.1046/j.1460-2695.2002.00506.x.

[24] S. Ţălu, R.S. Matos, E.P. Pinto, S. Rezaee, M. Mardani, Stereometric and fractal analysis of sputtered Ag-Cu thin films, Surf. Interfaces 21 (2020), 100650, https://doi.org/10.1016/j.surfin.2020.100650.
[25] A.T. Beyene, G. Belingardi, Bending fatigue failure mechanisms of twill fabric E-Glass/Epoxy composite, Compos. Struct. 122 (2015) 250–259, https://doi.org/10.1016/j.compstruct.2014.11.067.
[26] D. Zhang, S. Liu, B. Liu, J. Hong, Investigation on bending fatigue failure of a micro-gear through finite element analysis, Eng. Fail. Anal. 31 (2013) 225–235, https://doi.org/10.1016/j.engfailanal.2013.02.003.
[27] W. Macek, Fractal analysis of the bending-torsion fatigue fracture of aluminium alloy, Eng. Fail. Anal. 99 (2019) 97–107, https://doi.org/10.1016/j.engfailanal.2019.02.007.
[28] A.M. Vilardell, P. Krakhmalev, G. Fredriksson, F. Cabanettes, A. Sova, D. Valentin, P. Bertrand, Influence of surface topography on fatigue behavior of Ti6Al4V alloy by laser powder bed fusion, Procedia CIRP 74 (2018) 49–52, https://doi.org/10.1016/j.procir.2018.08.028.
[29] M. Tanaka, Y. Kimura, J. Taguchi, R. Kato, Fracture surface topography and fracture mechanism in austenitic SUS316 steel plates fatigued by repeated bending, J. Mater. Sci. 41 (2006) 2885–2893, https://doi.org/10.1007/s10853-005-5160-0.
[30] K. Shin, D. Kim, H. Park, M. Sim, H. Jang, J.I. Sohn, S.N. Cha, J.E. Jang, Artificial tactile sensor with pin-type module for depth profile and surface topography detection, IEEE Trans. Ind. Electron. 67 (2019) 637–646, https://doi.org/10.1109/TIE.2019.2912788.
[31] Whitehouse, D. Surface metrology today: Complicated, confusing, effective. In *Proceedings of the 13th International Conference on Metrology and Properties of Engineering Surfaces*, Twickenham Stadium, UK, 12–15 April 2011; pp. 1–10.
[32] W. Kapłonek, T. Mikolajczyk, D.Y. Pimenov, M.K. Gupta, M. Mia, S. Sharma, K. Patra, M. Sutowska, High-accuracy 3D optical profilometry for analysis of surface condition of modern circulated coins, Materials 13 (2020) 5371, https://doi.org/10.3390/ma13235371.
[33] P. Pawlus, R. Reizer, M. Wieczorowski, Problem of non-measured points in surface texture measurements, Metrol. Meas. Syst. 24 (2017) 525–536, https://doi.org/10.1515/mms-2017-0046.
[34] Liu W, Chen X, Zeng W, Sun W, Jiang X, Scott P, Lou S. FVM and XCT measurement of surface texture of additively manufactured parts. *2021 26th International Conference on Automation and Computing (ICAC)*, Portsmouth, United Kingdom, 2021, pp. 1-6. https://www.doi.org/10.23919/ICAC50006.2021.9594146.
[35] F.M. Ismail, K. Yanagi, A. Fujii, An outlier correction procedure and its application to areal surface data measured by optical instruments, Meas. Sci. Technol. 21 (2010), 105105, https://doi.org/10.1088/0957-0233/21/10/105105.
[36] P. Podulka, P. Pawlus, P. Dobrzański, A. Lenart, Spikes removal in surface measurement, J. Phys. Conf. Ser. 483 (2014), 012025, https://doi.org/10.1088/1742-6596/483/1/012025.
[37] S. Huang, M. Tong, W. Huang, X. Zhao, An isotropic areal filter based on high-order thin-plate spline for surface metrology, IEEE Access 7 (2019) 116809–116822, https://doi.org/10.1109/ACCESS.2019.2934724.
[38] ISO 2016 25178-600. *Geometrical Product Specification (GPS)—Surface Texture: Areal Part 600: Metrological Characteristics for Areal-Topography Measuring Methods.* International Organization for Standardization: Geneva, Switzerland, 2016.
[39] G. Maculotti, X. Feng, M. Galetto, R.K. Leach, Noise evaluation of a point autofocus surface topography measuring instrument, Meas. Sci. Technol. 29 (2018), 065008, https://doi.org/10.1088/1361-6501/aab528.
[40] P. De Groot, The meaning and measure of vertical resolution in optical surface topography measurement, Appl. Sci. 7 (2017) 54, https://doi.org/10.3390/app7010054.
[41] P. Podulka, Suppression of the high-frequency errors in surface topography measurements based on comparison of various spline filtering methods, Materials 14 (2021) 5096, https://doi.org/10.3390/ma14175096.
[42] J. Sun, Z. Song, G. He, Y. Sang, An improved signal determination method on machined surface topography, Precis. Eng. 51 (2018) 338–347, https://doi.org/10.1016/j.precisioneng.2017.09.004.
[43] M.Y. Zakharchenko, A.V. Kochetkov, P.M. Salov, O.V. Zakharov, New system of functional parameters for surface texture analysis, Mater. Today:. Proc. 38 (4) (2021) 1866–1870, https://doi.org/10.1016/j.matpr.2020.08.488.
[44] P. Podulka, The effect of surface topography feature size density and distribution on the results of a data processing and parameters calculation with a comparison of regular methods, Materials 14 (15) (2021) 4077, https://doi.org/10.3390/ma14154077.
[45] R. Abdalla, R.J. Mitchell, Y.F. Ren, Non-carious cervical lesions imaged by focus variation microscopy, J. Dent. 63 (2017) 14–20, https://doi.org/10.1016/j.jdent.2017.05.001.
[46] W. Kapłonek, K. Nadolny, G. Krolczyk, G.M. Królczyk, The use of focus-variation microscopy for the assessment of active surfaces of a new generation of coated abrasive tools, Meas. Sci. Rev. 16 (2016) 42–53, https://doi.org/10.1515/msr-2016-0007.
[47] T.Y. Lin, L. Blunt, K.J. Stout, Determination of proper frequency bandwidth for 3D topography measurement using spectral analysis, Part i: Isotropic Surfaces. *Wear* 166 (1994) 221–232, https://doi.org/10.1016/0043-1648(93)90265-N.
[48] T.V. Vorburger, H.G. Rhee, T.B. Renegar, J.F. Song, A. Zheng, Comparison of optical and stylus methods for measurement of surface texture, Int J Adv Manuf Technol 33 (2007) 110–118, https://doi.org/10.1007/s00170-007-0953-8.
[49] S. Fu, F. Cheng, T. Tjahjowidodo, Y. Zhou, D. Butler, A Non-Contact Measuring System for In-Situ Surface Characterization Based on Laser Confocal Microscopy, Sensors 18 (2018) 2657, https://doi.org/10.3390/s18082657.
[50] A. Jullien, M. Neradovskiy, M. Mitov, Hyperspectral topography of the twisted, cholesteric patterns of an insect cuticle under various conditions of helix obliquity, APL Photonics 5 (2020), 096102, https://doi.org/10.1063/5.0019039.
[51] Li Y, Shen F, Hu L, Lang Z, Liu Q, Cai F, Fu L. A Stare-down video-rate High-throughput Hyperspectral Imaging System and Its Applications in Biological Sample Sensing. *IEEE Sensors Journal* (early access) https://www.doi.org/10.1109/JSEN.2023.3308394.
[52] G. Kwiatkowski, D. Rozumek, Mechanical properties of explosion welded selected materials, Przegląd Mechaniczny LXXV(6) (2016) 23–29, https://doi.org/10.15199/148.2016.6.1.
[53] D. Rozumek, R. Bański, Crack growth rate under cyclic bending in the explosively welded steel/titanium bimetals, Mater. Des. 38 (6) (2012) 139–146, https://doi.org/10.1016/j.matdes.2012.02.014.
[54] D. Rozumek, G. Kwiatkowski, The influence of heat treatment parameters on the cracks growth under cyclic bending in St-Ti clad obtained by explosive welding, Metals 9 (2019) 338, https://doi.org/10.3390/met9030338.
[55] D. Rozumek, S. Faszynka, Surface cracks growth in aluminum alloy AW-2017A-T4 under combined loadings, Eng. Fract. Mech. 226 (2020), 106896, https://doi.org/10.1016/j.engfracmech.2020.106896.
[56] W. Macek, Post-failure fracture surface analysis of notched steel specimens after bending-torsion fatigue, Eng. Fail. Anal. 105 (2019) 1154–1171, https://doi.org/10.1016/j.engfailanal.2019.07.056.
[57] P. Podulka, W. Macek, R. Branco, R.M. Nejad, Reduction in errors in roughness evaluation with an accurate definition of the S-L surface, Materials 2023 (1865) 16, https://doi.org/10.3390/ma16051865.
[58] X. Jiang, N. Senin, P.J. Scott, F. Blateyron, Feature-based characterisation of surface topography and its application, CIRP Ann. 70 (2) (2021) 681–702, https://doi.org/10.1016/j.cirp.2021.05.001.
[59] P. Pawlus, R. Reizer, M. Wieczorowski, G.M. Krolczyk, Study of surface texture measurement errors, Measurement 210 (2023), 112568, https://doi.org/10.1016/j.measurement.2023.112568.
[60] P. Podulka, Reduction of influence of the high-frequency noise on the results of surface topography measurements, Materials 14 (2021) 333, https://doi.org/10.3390/ma14020333.
[61] Y. Kondo, I. Yoshida, D. Nakaya, M. Numada, H. Koshimizu, Verification of Characteristics of Gaussian Filter Series for Surface Roughness in ISO and Proposal of Filter Selection Guidelines, Nanomanuf Metrol 4 (2021) 97–108, https://doi.org/10.1007/s41871-021-00096-5.
[62] Y. Shao, F. Xu, J. Chen, J. Lu, S. Du, Engineering surface topography analysis using an extended discrete modal decomposition, J. Manuf. Process. 90 (2023) 367–390, https://doi.org/10.1016/j.jmapro.2023.02.005.
[63] B. He, H. Zheng, S. Ding, R. Yang, Z. Shi, A review of digital filtering in evaluation of surface roughness, Metrol. Meas. Syst. 28 (2021) 217–253, https://doi.org/10.24425/mms.2021.136606.
[64] D. Janecki, A two-dimensional isotropic spline filter, Precis. Eng. 37 (2013) 948–965, https://doi.org/10.1016/j.precisioneng.2013.05.005.
[65] D. Gogolewski, Fractional spline wavelets within the surface texture analysis, Measurement 179 (2021), 109435, https://doi.org/10.1016/j.measurement.2021.109435.
[66] S. Lou, X. Jiang, P.J. Scott, Application of the morphological alpha shape method to the extraction of topographical features from engineering surfaces, Measurement 46 (2013) 1002–1008, https://doi.org/10.1016/j.measurement.2012.09.015.
[67] H. Hanada, T. Saito, M. Hasegawa, K. Yanagi, Sophisticated filtration technique for 3D surface topography data of rectangular area, Wear 264 (2008) 422–427, https://doi.org/10.1016/j.wear.2006.08.035.
[68] ISO 16610-31:2016; *Geometrical Product Specifications (GPS)—Filtration—Part 31: Robust Profile Filters: Gaussian Regression Filters.* International Organization for Standardization: Geneva, Switzerland, 2016.
[69] Y. Shao, S. Du, H. Tang, An extended bi-dimensional empirical wavelet transform based filtering approach for engineering surface separation using high definition metrology, Measurement 178 (2021), 109259, https://doi.org/10.1016/j.measurement.2021.109259.
[70] P. Wüst, A. Edelmann, R. Hellmann, Areal Surface Roughness Optimization of Maraging Steel Parts Produced by Hybrid Additive Manufacturing, Materials 13 (2020) 418, https://doi.org/10.3390/ma13020418.
[71] X. Jiang, N. Senin, P.J. Scott, F. Blateyron, Feature-based characterisation of surface topography and its application, CIRP Ann-Manuf. Tech. 70 (2021) 681–702, https://doi.org/10.1016/j.cirp.2021.05.001.
[72] P. Pawlus, W. Graboń, The method of truncation parameters measurement from material ratio curve, Precis. Eng. 324 (2008) 342–347, https://doi.org/10.1016/j.precisioneng.2008.01.002.
[73] P. Pawlus, Change of cylinder surface topography in the initial stage of engine life, Wear 209 (1997) 247–254, https://doi.org/10.1016/S0043-1648(97)00007-0.
[74] W. Macek, R. Branco, J.D. Costa, C. Pereira, Strain sequence effect on fatigue life and fracture surface topography of 7075–T651 aluminium alloy, Mech. Mater. 160 (2021), 103972, https://doi.org/10.1016/j.mechmat.2021.103972.